Mon. Not. R. Astron. Soc. **265,** 946–967 (1993)

Wind accretion in binary stars – I. Intricacies of the flow structure

T. Theuns[1,2]★ and A. Jorissen[2]†‡
[1] *Scuola Normale Superiore, Piazza dei Cavalieri 7, I-56126 Pisa, Italy*
[2] *European Southern Observatory, Karl-Schwarzschild-Straße 2, D-85748 Garching bei München, Germany*

Accepted 1993 June 23. Received 1993 April 12; in original form 1992 December 2

ABSTRACT
The 3D flow structure of wind accretion in a binary system is computed numerically using SPH, taking into account binary rotation as well as wind acceleration. In the adiabatic $\gamma = 1.5$ model, high temperatures are reached in a bow shock close to the accreting star. This region could be responsible for the UV emission observed in such systems. In the isothermal model, the bow shock is no longer detached. Moreover, an accretion disc forms around the star. The disc is inclined with respect to the orbital plane and is in differential rotation. The flow structure is considerably more complicated than in the simple plane-parallel picture that is usually employed to describe these systems.

Key words: accretion, accretion discs – hydrodynamics – binaries: close – stars: mass-loss.

1 INTRODUCTION

Because the main-sequence lifetime of a star depends strongly on its mass, the more massive (or 'primary') component of a binary system will evolve faster than the less massive one (the 'secondary'). During its late evolutionary stages, the primary component may suffer from a severe mass loss, and part of the matter lost by the primary can then be accreted by the secondary. Accretion of this matter is likely to alter the chemical composition of the surface layers of the secondary component. Changes in the orbital parameters of the binary as well as in the spin properties of the components may also occur. The mass transfer itself is usually considered in either of two modes: Roche-lobe overflow (e.g. Paczyński 1971) or wind accretion (Hunt 1971; Sawada, Matsuda & Hachisu 1986; Anzer, Börner & Monaghan 1987; Sawada et al. 1989). In the first mode, after the primary has swollen to fill the critical Roche surface surrounding it, even zero-velocity gas from the surface of the star can fall into the potential well of the secondary. Dissipation in this gas will lead eventually to its accretion by the secondary. Note that, in principle, no mass is lost from the binary system in this case. Moreover, since the primary must reach a radius that is a substantial fraction of the binary separation, tidal effects will be important, leading to the synchronization of the spin of the primary with the orbital rotation, as well as to orbital circularization (e.g. Tassoul 1987). As far as wind accretion is concerned, the primary does not fill its Roche lobe but is subject instead to a stellar wind (see also Tout & Hall 1991 for the analysis of the mixed case of wind-driven Roche-lobe overflow). For 'low' wind speeds, gas can reach the secondary only by passing through the inner Lagrangian point. With increasing wind speed, the route to the secondary does not necessarily have to pass through the Lagrangian point, but gas still cannot escape to infinity. Finally, for even higher speeds, gas may partly be accreted by the secondary, and partly escape to infinity. In this paper, we focus on the last case.

The outcome of binary evolution through Roche-lobe overflow will be very different from that through wind accretion. First, the amount of accreted matter will in general be larger in the Roche-lobe-overflow mode. Moreover, as will be shown in Theuns & Jorissen (in preparation, Paper II), wind accretion tends to decelerate the secondary component and thus to increase the eccentricity (Huang 1956), while Roche-lobe overflow leads to orbital circularization. Finally, since the bulk of the mass lost by wind is not accreted by the secondary but escapes from the system, wind mass loss is likely to increase the binary separation (at least when neglecting any spin–orbit angular momentum transfer), whereas shrinking orbits may instead result from Roche-lobe overflow (see e.g. Savonije 1983).

Wind accretion can pollute the surface layers of the secondary component even in relatively wide binaries. In this context, wind accretion has been invoked to explain the chemically peculiar nature of barium stars (Boffin & Jorissen

★ E-mail address: theuns@vaxsns.dnet%ux1sns.sns.it.
†E-mail address: ajorisse@astro.ulb.ac.be.
‡Present address: Institut d'Astronomie et d'Astrophysique, Université Libre de Bruxelles C.P. 165, Av. F. Roosevelt 50, B-1050 Bruxelles, Belgium.

1988), which prompted the present investigation. The observed enhancement of carbon and heavy elements like barium in the envelopes of these stars is interpreted as being due to the accretion of material from the envelope of the former asymptotic giant branch (AGB) companion, which now has evolved into a white dwarf (WD). Indeed, there is evidence that all Ba stars with strong chemical anomalies are members of a binary system (McClure & Woodsworth 1990; Jorissen & Mayor 1988, and in preparation). In this paper we shall focus on the dynamical aspects of the wind accretion model, and in a follow-up paper we shall discuss the results in the context of Ba stars.

A key question in the context of wind accretion concerns the amount of matter that can be accreted by the secondary which is orbiting in the bubble of gas blown by the primary. In the simplest form of the accretion problem, a (single) star with mass M moves at constant velocity V through gas of initially uniform sound speed c and density ρ. This case was studied first by Bondi & Hoyle (1944) and Bondi (1952), who suggested $\dot{M}=\alpha 2\pi\rho(GM)^2/(V^2+c^2)^{3/2}$ for the accretion rate, where α is a constant of order unity. The validity of this approximation for $\dot{M}$ has been extensively tested using numerical simulations in two dimensions (e.g. Hunt 1971; Anzer et al. 1987; de Kool & Savonije 1988) and in three dimensions (Livio et al. 1986; Sawada et al. 1989; Matsuda et al. 1992; Sawada & Matsuda 1992). High-resolution 2D simulations (see e.g. Livio 1992) found the flow pattern to be unstable, but the 3D simulations by Sawada et al. (1986) or Boffin (1992) always reached a steady state. In some simulations, the incoming gas had a velocity and/or density gradient, to approximate the true geometry of accretion in a binary system. Biermann (1971) used the method of characteristics in 2D geometry to obtain the flow pattern in the supersonic domain, *including* the binary rotation. 2D simulations in a rotating frame were also presented by Sørensen, Matsuda & Sakurai (1975) and by Matsuda, Inoue & Sawada (1987).

In this paper, we present fully 3D smoothed particle hydrodynamics (SPH) simulations of wind accretion in a binary, integrating over several orbital periods with up to 40 000 particles. We consider the case where wind speed and orbital velocity are of the same order of magnitude. The geometry of the wind flow can then be expected to be very different from the plane-parallel Bondi & Hoyle geometry. There is thus no guarantee that the above formula holds in the situation considered, and this will be checked in Paper II by comparing the accretion rate derived from the present calculations to that derived from the Bondi & Hoyle formula. The present calculations also simulate the acceleration mechanism of the wind from the red giant. Section 2 describes the model and the computational approach in more detail. The flow pattern is discussed in Section 3. Section 4 compares some observational diagnostics of wind accretion with the results of our simulation. Finally, Section 5 presents a summary.

2 ASSUMPTIONS AND COMPUTATIONAL APPROACH

2.1 Equations

We describe the hydrodynamics of the gas by the following standard set of equations:

$$\frac{d\rho}{dt}=-\rho \operatorname{div} \boldsymbol{v}, \tag{1}$$

$$\frac{d\boldsymbol{v}}{dt}=-\frac{M_2}{r_2^3}\boldsymbol{r}_2-\frac{M_1(1-f)}{r_1^3}\boldsymbol{r}_1-\frac{1}{\rho}\operatorname{grad} p, \tag{2}$$

$$\frac{du}{dt}=-\frac{p}{\rho}\operatorname{div} \boldsymbol{v}, \tag{3}$$

$$p=(\gamma-1)\rho u \tag{4}$$

$$=\kappa\rho^{\gamma}, \tag{5}$$

where p, ρ and u are respectively the gas pressure, density and thermal energy per unit mass. The gas velocity (in an inertial frame) is denoted by $\boldsymbol{v}$ and d/dt is the Lagrangian time derivative. The first term on the right-hand side of equation (2) is the acceleration of the gas due to the gravitational attraction of the secondary (of mass M_2), hence $\boldsymbol{r}_2$ connects the centre of mass of the secondary star with the fluid element (the gravitational constant is taken equal to 1). The next term in equation (2) denotes the analogous term for the primary (of mass M_1), where the factor $(1-f)$ simulates the acceleration mechanism for the wind (see Section 2.5).

As equation (4) shows, we assume further that the gas is ideal, with polytropic index γ (equation 5), so that $u=\Re T/\mu(\gamma-1)$, where $\Re$ is the perfect gas constant, T is the temperature and μ is the mean molecular weight per particle. The sound speed is computed from $c^2=(\gamma-1)\gamma u$. For an isothermal gas, $\gamma=1$ in equation (5), whereas equation (4) is replaced by $p=c^2\rho$, c being the isothermal sound speed. We performed simulations with $\gamma=1.5$ and 1, so our results probably bracket the behaviour of the gas, if a realistic equation of state (i.e. including cooling) is used. Finally, note that self-gravity of the gas is neglected.

2.2 Numerical approach

We simulate the hydrodynamics of the gas using the Lagrangian particle method of smoothed particle hydrodynamics (Lucy 1977; Gingold & Monaghan 1977) in an implementation very similar to the one described and tested by Theuns (1992). The SPH estimate of the density ρ at the position $\boldsymbol{r}_i$ of particle i is obtained from

$$\rho(\boldsymbol{r}_i)=\sum_j m_j W\left(\frac{|\boldsymbol{r}_i-\boldsymbol{r}_j|}{(h_i+h_j)/2}\right), \tag{6}$$

where m_j is the 'mass' of particle j, $W(x)$ is the spline function described by Monaghan (1985) and h_i denotes the local 'resolution' around particle i. The latter is chosen to ensure that, on average, 50 particles contribute to the sum in equation (6) [$W(x)=0$ for $x\geq 2$].

In order to be able to simulate shocks, we include the artificial viscosity terms as described by Lattanzio et al. (1986). We employ an explicit, predicted-mid-point time-stepping scheme which is accurate to second order and has a uniform time-step. For recent reviews of SPH, see e.g. Monaghan (1988) and Benz (1989).

In equation (2), we smooth the gravitational forces M/r^2 by replacing r^2 by $r^2+\varepsilon^2+h^2$, where ε is constant and h is the local resolution.

In order to avoid an N^2 (N being the total number of particles) calculation to evaluate the sum in equation (6), two 'neighbour-finding' algorithms are in common use: a linked list (see e.g. Hockney & Eastwood 1981) and a hierarchical tree scheme (Hernquist & Katz 1989). However, the efficiency of both these schemes is reduced in cases where the range in h becomes large. In the Appendix, we describe a new multi-grid scheme for evaluating the sum in equation (6) that does not suffer from a large range in h and additionally requires very little overhead.

For display purposes (Section 3), we compute contours of state variables (e.g. density, sound speed, etc.) by interpolating these variables to vertices of a square grid, using an equation like equation (6), where 'particle' i is the massless grid vertex. We typically use 200 vertices in each Cartesian direction. Note that this grid is used only for display purposes: the simulation itself remains fully Lagrangian.

2.3 Boundary and initial conditions

The two stars move on an unperturbed binary orbit with semimajor axis a, eccentricity e and period P, which are all kept constant during the simulation. The masses M_1 and M_2 are also kept constant. Around star 1, a spherically symmetric wind is simulated in the following way. SPH particles are generated on the vertices of a grid, but only particles in a shell between r_a and r_b around the mass-losing star are retained ($r_a < r_b$). These particles are given a constant mass (but the grid is stretched so that $\rho \propto 1/r^2$), a constant thermal energy u and outward radial velocity v_w. As soon as they pass a third radius $r_c > r_b$, they start obeying equations (1) to (5). When there are no more particles left between r_a and r_b, a new set is injected. In the case of a single star, we find that the wind that is generated in this way follows closely the exact solution for a spherically symmetric, stationary outflow, as long as the sonic point is inside r_c. Note that, in the binary case, gas inside r_c also inherits the translational velocity of the mass-losing star, which is not spinning.

Accretion by the secondary is simulated in the following way. Ideally, we would like the gas to obey equations (1) to (5) up to the stellar surface, at which point it can be removed from the calculation, since it is accreted by that star. However, for a typical binary separation of, say, $a = 3$ au and a stellar radius of $R_2 = 1\,\mathrm{R}_\odot$, the ratio a/R_2 amounts to ≈ 640. This means that, even using variable resolution, we cannot hope to resolve the stellar surface in our calculation (and so our simulation cannot distinguish between accretion by a main-sequence star and that by a white dwarf). We therefore proceed as follows: let $\bar{h}$ be the average resolution around the accreting star computed in a sphere of radius r_h; then

$$\frac{\mathrm{d}m_i}{\mathrm{d}t} = \min\left[-\frac{m_i(1 - r_2^2/\bar{h}^2)}{\mathrm{d}t}, 0\right], \tag{7}$$

where $\mathrm{d}m_i/\mathrm{d}t$ is the change in mass m_i of the SPH particle and $\mathrm{d}t$ is the time-step (see also Anzer et al. 1987). The recipe (7) for accretion ensures that no pressure builds up around the accreting star, which would cause a decrease in the accretion rate, i.e. the secondary accretes as a black hole would. Particles are removed from the calculation when their mass is a small fraction (0.1 per cent) of the original mass. Finally, particles are also removed from the calculation once they cross an outer, spherical boundary, which is located at $3a$. Since the flow is (highly) supersonic there, this boundary condition does not influence the inner flow characteristics. Moreover, this boundary lies well within the centrifugal tail of the equipotential curves, so that particles reaching it will not come back.

We start the simulation by inserting particles between r_a and r_b. We do this at rather low resolution (i.e. a small number of particles are inserted). After a stationary state is reached (we ran the simulation for 12 periods in the adiabatic case, and for 20 in the isothermal one), we increase the resolution by inserting more particles whenever the region $r_a < r < r_b$ is empty (but these particles have a lower mass, so the mass-loss rate does not change). This has the advantage of speeding up the calculation as well as providing a handle on how much the results depend on resolution. In our highest resolution simulations (containing about 4×10^4 particles), the time-step (which is limited by the Courant condition for stability reasons) is $\Delta t \approx 0.3 \times 10^{-3} P$, so simulation of the system over several periods is extremely CPU-time-consuming at this resolution. We ran the simulations at the highest resolution over two periods, requiring several days of CPU-time on the Stardent GS1000 computer at the European Southern Observatory (ESO).

2.4 Estimation of accretion rates

The accretion rates per unit volume of mass, $\dot{m}$, momentum, $\dot{\boldsymbol{p}}$, energy, $\dot{e}$, and spin, $\dot{\boldsymbol{s}}$, are defined in the rotating frame through

$$\frac{\mathrm{D}\rho}{\mathrm{D}t} + \operatorname{div} \rho \boldsymbol{v}_r = \dot{m}, \tag{8}$$

$$\frac{\mathrm{D}\rho \boldsymbol{v}_r}{\mathrm{D}t} + \operatorname{div} \rho \boldsymbol{v}_r \boldsymbol{v}_r + \rho(\boldsymbol{F}_\omega - \boldsymbol{F}) = \dot{\boldsymbol{p}}, \tag{9}$$

$$\frac{\mathrm{D}}{\mathrm{D}t}\left(\frac{1}{2}\rho v_r^2 + \rho u + \rho\phi\right) + \operatorname{div}\left(\frac{1}{2}\rho v_r^2 + \rho u + \rho\phi + p\right)\boldsymbol{v}_r + \rho \boldsymbol{v}_r \cdot \boldsymbol{F}_\omega = \dot{e}, \tag{10}$$

$$\frac{\mathrm{D}}{\mathrm{D}t}\rho \boldsymbol{h} + \operatorname{div} \rho \boldsymbol{h} \boldsymbol{v}_r + \rho(\boldsymbol{F}_\omega - \boldsymbol{F}) \times \boldsymbol{r}_2 = \dot{\boldsymbol{s}}, \tag{11}$$

where $\boldsymbol{v}_r = \boldsymbol{v} - \boldsymbol{\omega} \times \boldsymbol{r}$ is the velocity in the frame rotating with angular velocity $\omega = 2\pi/P$, $\boldsymbol{r}$ is the position vector with respect to the centre of mass of the system, and $\boldsymbol{h} = \boldsymbol{v}_r \times \boldsymbol{r}_2$ is the angular momentum per unit mass. The time derivative $\mathrm{D}/\mathrm{D}t = \partial/\partial t + (\boldsymbol{\omega} \times \boldsymbol{r}) \cdot \operatorname{grad}$ is the Eulerian time derivative in the rotating frame. We also define the total force $\boldsymbol{F}$ and 'pseudo-force' $\boldsymbol{F}_\omega$ as

$$\boldsymbol{F} = -\operatorname{grad} \phi - \frac{1}{\rho} \operatorname{grad} p, \tag{12}$$

$$\boldsymbol{F}_\omega = 2\boldsymbol{\omega} \times \boldsymbol{v}_r + \boldsymbol{\omega} \times (\boldsymbol{\omega} \times \boldsymbol{r}) + \dot{\boldsymbol{\omega}} \times \boldsymbol{r}, \tag{13}$$

where ϕ denotes the gravitational potential of the two stars (but including the correction factor f accounting for the wind acceleration process). Note that the Coriolis force (the first term in equation 13) does not contribute to the heating in equation (10), since $\boldsymbol{v}_{\rm r}\cdot(\boldsymbol{\omega}\times\boldsymbol{v}_{\rm r})=0$. The total accretion rates can be obtained from

$$\dot{M}=\sum_i \frac{\mathrm{d}m_i}{\mathrm{d}t} \tag{14}$$

$$\dot{\boldsymbol{P}}=\sum_i \frac{\mathrm{d}m_i}{\mathrm{d}t}\boldsymbol{v}_{\mathrm{r},i} \tag{15}$$

$$\dot{E}=\sum_i \frac{\mathrm{d}m_i}{\mathrm{d}t}\left(\frac{1}{2}\boldsymbol{v}_{\mathrm{r},i}^2+u_i+\phi_i\right) \tag{16}$$

$$\dot{\boldsymbol{S}}=\sum_i \frac{\mathrm{d}m_i}{\mathrm{d}t}\boldsymbol{h}_i. \tag{17}$$

Alternatively, in a stationary flow, they may be obtained by integrating the divergence terms appearing in equations (8)–(11) over a sphere centred on the accreting star. By applying Gauss's theorem, these divergence terms can also be obtained by integrating $\boldsymbol{\Phi}\cdot\mathrm{d}\boldsymbol{S}$ over the surface of such a sphere. Here, $\mathrm{d}\boldsymbol{S}$ denotes the outward surface element and $\boldsymbol{\Phi}$ the flux vector. We obtained the local flux $\boldsymbol{\Phi}$ of a quantity A using the SPH estimate at the position $\boldsymbol{r}_i$ at which the flux is evaluated:

$$\boldsymbol{\Phi}(A)_i=\sum_j m_j\boldsymbol{v}_j A_j W\left(\frac{|\boldsymbol{r}_i-\boldsymbol{r}_j|}{h_j}\right)\Big/\rho_j. \tag{18}$$

We took typically 400 points equally spaced in cos θ and φ to evaluate $\boldsymbol{\Phi}$, which we then integrated over the surface of the sphere (θ and φ are spherical coordinates with respect to the centre of the sphere). We computed these fluxes at every time-step over spheres of radii $0.5r_h$, r_h and $1.5r_h$. Constancy of the accretion rates computed in such a way means that a steady state has been reached (Paper II).

2.5 Dimensional units and scaling

As an illustrative example, we use the following 'typical' dimensional values for the binary components: $M_1=3\,\mathrm{M}_\odot$, $M_2=1.5\,\mathrm{M}_\odot$, $R_1=200\,\mathrm{R}_\odot$ for the radius of the giant, and $R_2=1\,\mathrm{R}_\odot$ for the radius of the accreting star. The orbit is taken to be circular ($e=0$). For a binary separation of $a=3$ au, the period then amounts to $P=895$ d and the orbital speed to $v_{\rm orb}=36$ km s^{-1}. Finally, we adopt a wind speed of $v_{\rm w}=15$ km s^{-1}, as indicated by the observations of single red giant winds (e.g. Knapp & Morris 1985), and a mass-loss rate $\dot{M}_1=10^{-6}\,\mathrm{M}_\odot\,\mathrm{yr}^{-1}$. Note that an acceleration mechanism (represented in our treatment by the parameter f in equation 2) is needed in order to drive the wind to infinity, since the escape velocity from the mass-losing star is about $5v_{\rm w}$. Detailed models of mass loss from red giants (e.g. Bowen 1988) indicate that the wind acceleration probably results from a two-step process. Shock waves associated with the stellar pulsation first lift matter from the red giant surface to regions where dust can form (at a few stellar radii from the photosphere). Radiation pressure on dust then provides a further thrust, the gas being carried away with the dust to an altitude where the escape velocity finally drops below the wind velocity. Bowen's models predict that the wind already reaches its terminal velocity at very low altitude, in regions where that velocity is still smaller than the escape velocity. In our numerical description of the wind mass loss, it was therefore assumed that the wind acceleration mechanism exactly balances the gravitational attraction of the mass-losing star from the photosphere onwards (i.e. $f=1$ in equation 2), thus yielding a constant wind velocity as found by Bowen (1988; see also fig. 5a of Gail & Sedlmayr 1987, who found the radiative acceleration of the wind to be as large as 4 times the gravitational deceleration). It has to be emphasized that this choice in fact suppresses the gravitational pull of the mass-losing star on the flowing gas over the whole region considered. This implicitly assumes that the presence of the accreting star does not prevent the formation of dust in the wind, since dust constitutes the driving force of the wind in regions out of the reach of the pulsations of the mass-losing star.

The sound speed in the wind close to the mass-losing star is $v_{\rm w}/10$, so the wind leaves the star in the supersonic regime. Two cases were considered, an adiabatic one ($\gamma=1.5$ in equation 4) and an isothermal one ($\gamma=1$), all other parameters being the same. These values should bracket the real situation.

In the following, dimensionless quantities are used such that $G=a=P=1$ (G is the gravitational constant). For the particular parameter values adopted here, this choice corresponds to $0.114\,\mathrm{M}_\odot$ as the unit of mass, $4.65\times10^{-2}\,\mathrm{M}_\odot\,\mathrm{yr}^{-1}$ as the unit of mass-loss rate, 5.8 km s^{-1} as the unit of velocity, 2.5×10^{-6} kg m^{-3} as the unit of density (corresponding to 1.5×10^{15} particle cm^{-3}) and 3 au as the unit of distance. In dimensionless units the parameters $r_{\rm a}$, $r_{\rm b}$, $r_{\rm c}$, r_h and ε are 0.12, 0.25, 0.3, 0.3 and 0.05 respectively. We took the standard values $\alpha=\beta=1$ for the coefficients of the numerical viscosity (see Monaghan & Varnas 1988 for the definition of α and β).

3 THE FLOW PATTERN

3.1 The adiabatic model

The flow pattern of the adiabatic model is illustrated in Figs 1 to 3. All frames have been rotated so that the mass-losing star is located at ($x=0.33$, $y=0$, $z=0$) and the accreting star at ($x=-0.66$, $y=0$, $z=0$), where x–y defines the orbital plane.

Fig. 1(a) shows the velocity profile in the orbital plane and in a rotating frame in which the two stars are at rest: the velocity vectors shown are $\boldsymbol{v}_{\rm r}$ [as defined after equation (11); note that only 1/2 of the particles are shown]. We will refer to this non-inertial frame as the 'stationary frame'. Figs 1(b) and (c) show the corresponding density and sound speed distributions. The mass-losing star is surrounded on the right-hand side by a 'spiral arm' emerging from a 'stagnation point' at $x\approx-0.2$, $y\approx0.5$ (Fig. 1a). This spiral arm arises from the collision between gas expanding away from the stagnation point and gas expanding away from the primary. The origin of the stagnation point itself can best be understood by looking at the flow structure in the x–z plane (see below). We shall refer to gas streams following this spiral pattern as the 'spiral-arm stream'.

The gas flow in the direction of the secondary (i.e. at about $x\approx-0.5$, $y\approx0$; see Fig. 1a) is strongly perturbed by the gravitational attraction of star 2. At first ($x\geq-0.5$, $y\approx0$) it is

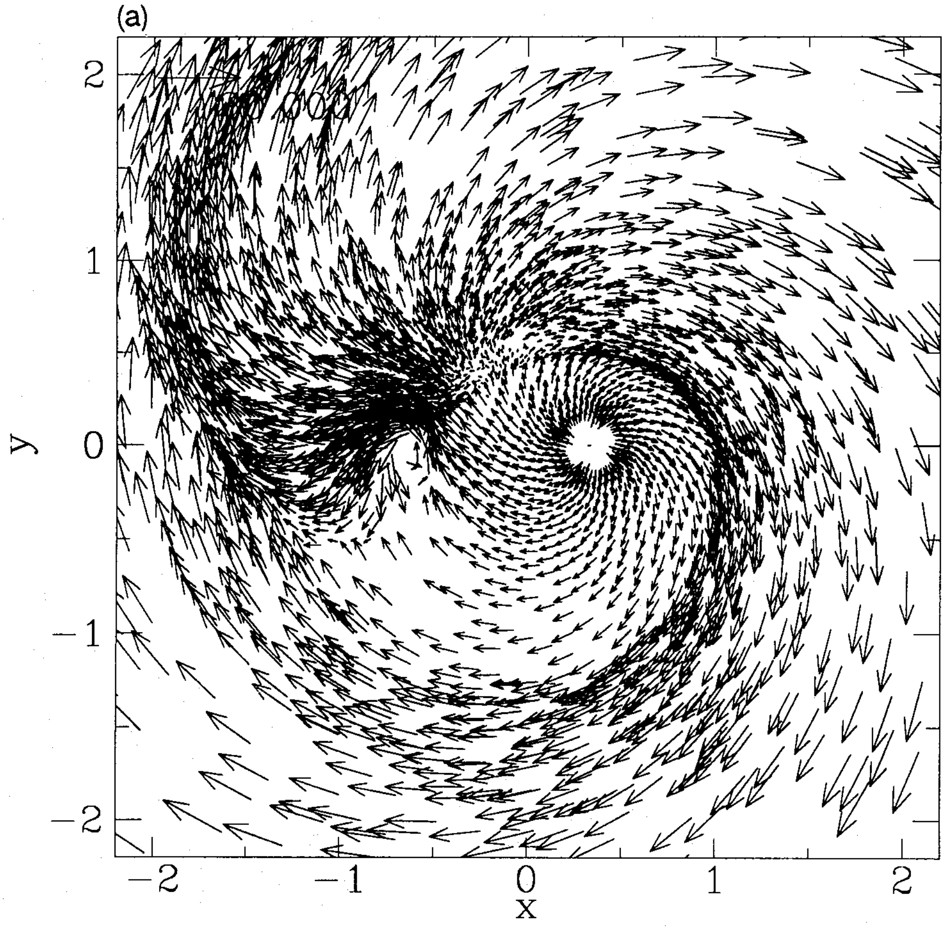

Figure 1. Flow structure in the stationary (x–y) plane for the adiabatic $\gamma = 1.5$ model. The mass-losing star is at ($x = 0.33$, $y = 0$, $z = 0$), and the accreting star at ($x = -0.66$, $y = 0$, $z = 0$). Note that the mass-losing star has a radius of 0.3, but particles are injected at a radius of 0.12 (Section 2.5). (a) The velocity structure: 1/2 of all particles in the z-slice $[-0.1, 0.1]$ enclosing the orbital plane are shown. (b) Grey-scale representation of the density with contour lines added. The start, end and step of the contours are indicated. The grey-scale ranges linearly from 0 to 6E-6. (c) As (b) but for the sound speed, with grey-scale from 0 to 3.8.

moving with positive y velocity. This velocity is, however, reversed later due to the gravitational force from the secondary, and the flow moves with $v_y < 0$ at $x \approx -0.9$, $y \approx 0$. We shall refer to this stream as the 'Roche-lobe' (RL) stream.

The spiral-arm and RL streams collide, causing a shock to the left of the accreting star ($x \approx -1.5$, $y \geq -0.2$), as can be seen from Figs 1(b) and (c).

Figs 2(a)–(c) illustrate the flow pattern in the x–z plane at $y = 0$. The diverging gas stream leaving the primary (located at $x = 0.33$, $y = 0$) is clearly seen on the right-hand side. Gas expanding away from the primary and having $v_x < 0$ is the RL stream introduced in Fig. 1(a). Three effects conspire to keep this stream confined to the orbital plane $z = 0$. First, the RL stream is hampered from moving away from the orbital plane by gas raining down on to this plane (see the gas flow at $x \approx -0.8$, $z = \pm 0.5$ in Fig. 2a). Secondly, the gravitational force of the secondary tries to compress the RL stream in the z-direction, causing the stream to pass through a 'gravitational funnel', at $x \approx -0.67$, $z = 0$. Thirdly, the RL stream coming out of this funnel is confined to the orbital plane by two pockets of high-temperature gas at $x \approx -1.0$, $z = \pm 0.3$, placed symmetrically above and below the $z = 0$ plane. These hot pockets are due to a bow shock in the y–z plane, which we shall illustrate in Fig. 3.

The confined RL stream gives rise to the high-density 'tail' downstream (i.e. at $y > 0$) from the secondary in Figs 2(b) and 3(b), close to the $z = 0$ orbital plane. This tail also shows up in the corresponding sound speed plots 2(c) and 3(c), since the compression also heats the gas. The interaction between the RL and spiral-arm streams is responsible for the stagnation point of Fig. 1(a), as we show below. We note that the $v_x < 0$, $|z| < 0.2$ RL stream and the $v_x > 0$, $|z| > 0.5$ spiral-arm stream give rise to a vortex-like structure in Fig. 2(a).

Figs 3(a)–(c) depict the flow pattern in the y–z plane at $x = -0.66$ (i.e. including star 2). In this plane, the flow structure is reminiscent of the flow structure in the plane-parallel case. Gas is deflected from its orbit and a detached bow shock forms around the accreting star (Fig. 3c). Fig. 3(b) shows the high-density wings of the bow shock and Fig. 3(c) the high-temperature post-shock gas. It is the high thermal

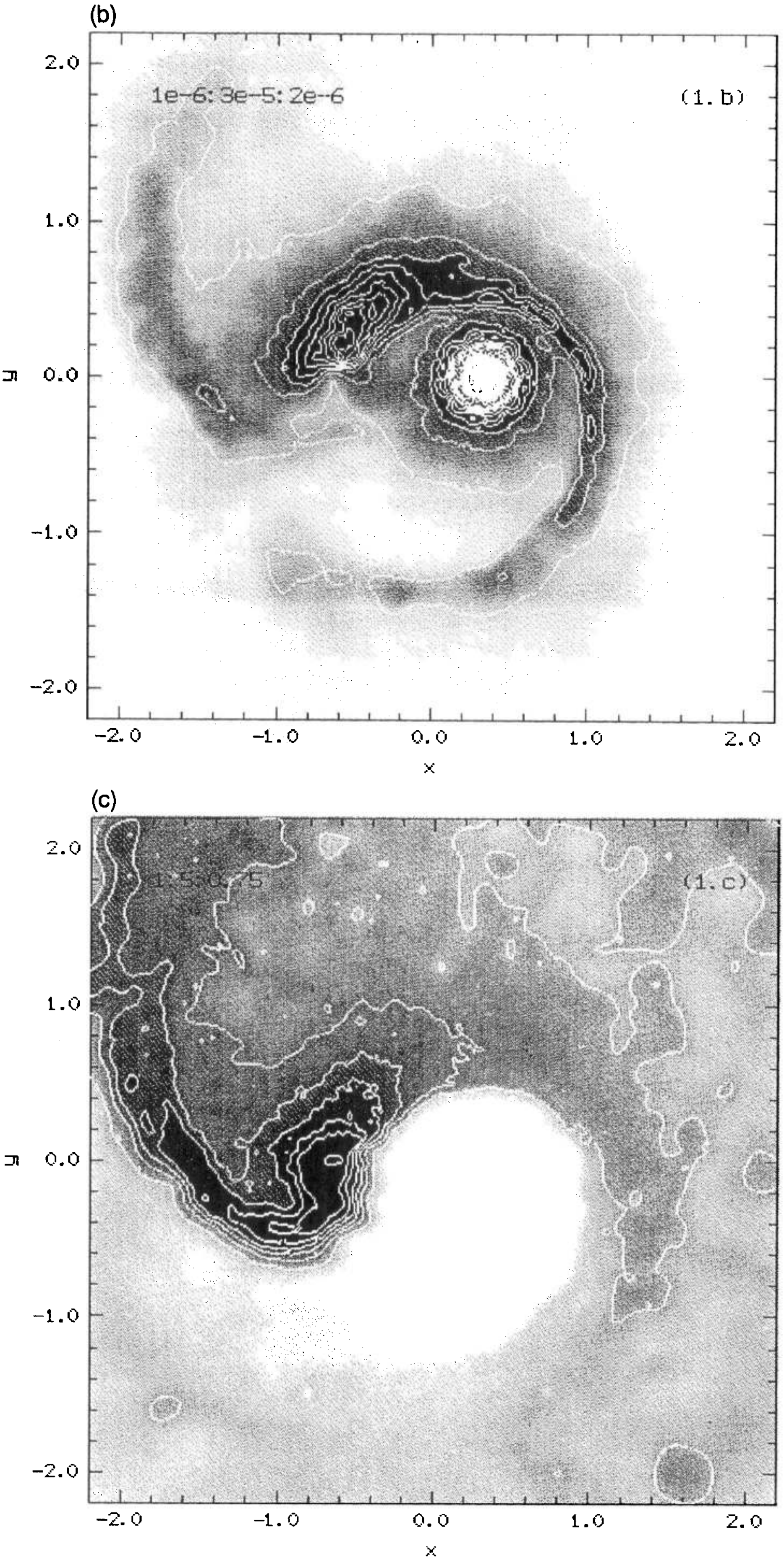

Figure 1 – *continued*

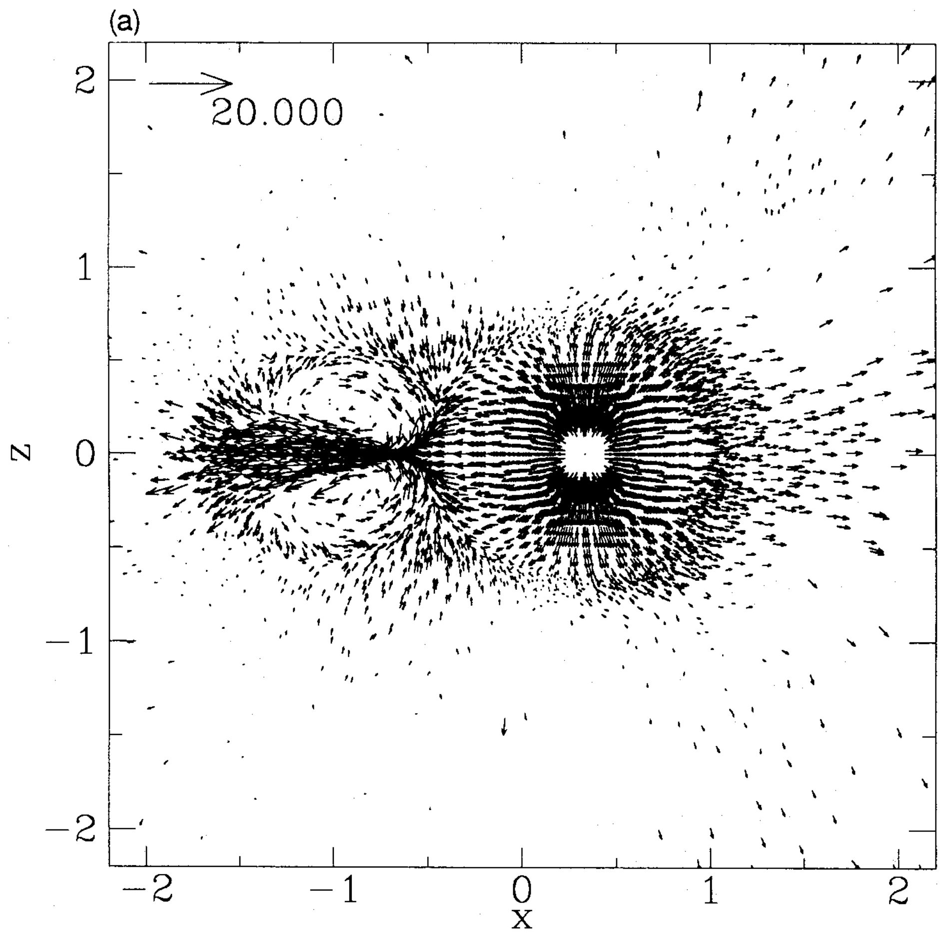

Figure 2. As Fig. 1 but for the $(x–z)$ plane. (a) shows all particles in a y-slice $[-0.1, 0.1]$.

pressure of the shocked gas that supports the bow shock against ram pressure. Note that the high-temperature region has already started at $y \approx -0.4$, well in front of the accreting star. The regions of high temperature at $y \approx 0$, $|z| < 0.5$ correspond to the pockets surrounded by the vortex lines in Fig. 2(a). The high temperature in this region is partly responsible for the confinement of the RL stream to the orbital plane. The density in this RL stream ($|z| < 0.2$, $y \geq 0$) is higher but the temperature lower than that of the gas that has passed through the bow shock ($|z| > 0.2$, $y > 0$, see Figs 3b and c). These two different regions can also be clearly distinguished in Fig. 3(a).

The overall flow pattern is considerably more complex than in the plane-parallel case. Its structure is really three-dimensional and hard to capture by displaying only a few two-dimensional cuts. The flow in the $x–z$ plane is reminiscent of that in the $y–z$ plane displayed in Fig. 3. There are important differences, however. In the $y–z$ plane, the bow shock is caused by the collision between the $z > 0$ and $z < 0$ components of the spiral arm, deflected by the gravitational attraction of star 2. This focusing of the $|z| > 0$ spiral-arm stream towards the orbital plane is also seen in the $x–z$ plane. In this plane, the stream converging in z and moving with $v_x > 0$ additionally collides with gas expanding away from star 1. For $y \lesssim 0.1$ like in Fig. 2(a), the ram pressure of the Roche-lobe flow is high and the Roche-lobe flow moves to negative x almost unimpeded. For larger y, however, the Roche-lobe flow is decelerated more and more (compare Fig. 4a with b). We note, moreover, that due to the orbital motion the focusing of gas from large $|z|$ tends to lag behind star 2. This delay explains the position of the shock responsible for the stagnation point behind and to the right of the accreting star (as seen in the orbital plane; Fig. 1a). This effect is very clearly seen in Fig. 4(b), which shows that gas flows from $|z| > 0$ towards the orbital plane to a position occupied by the accreting star about one-eighth of an orbital period earlier.

Figs 5(a) and (b) further illustrate the flow structure. Fig. 5(a) shows state variables along the line $x = -0.66$, $z = 0$ through the accreting object. Oncoming gas shocks to high temperatures in the detached bow shock. Such a detached bow shock was also found in the 2D plane-parallel simulations of Shima et al. (1985). Moving into the bow shock, density and pressure increase at nearly constant temperature.

(b)

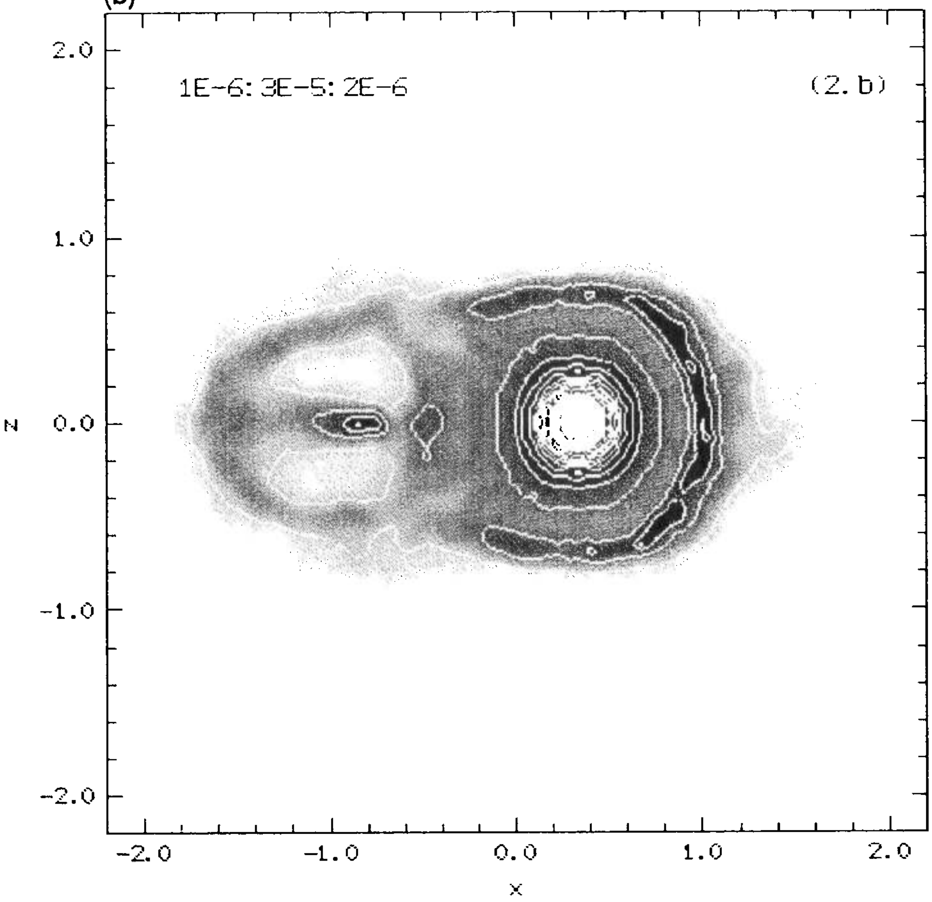

(c)

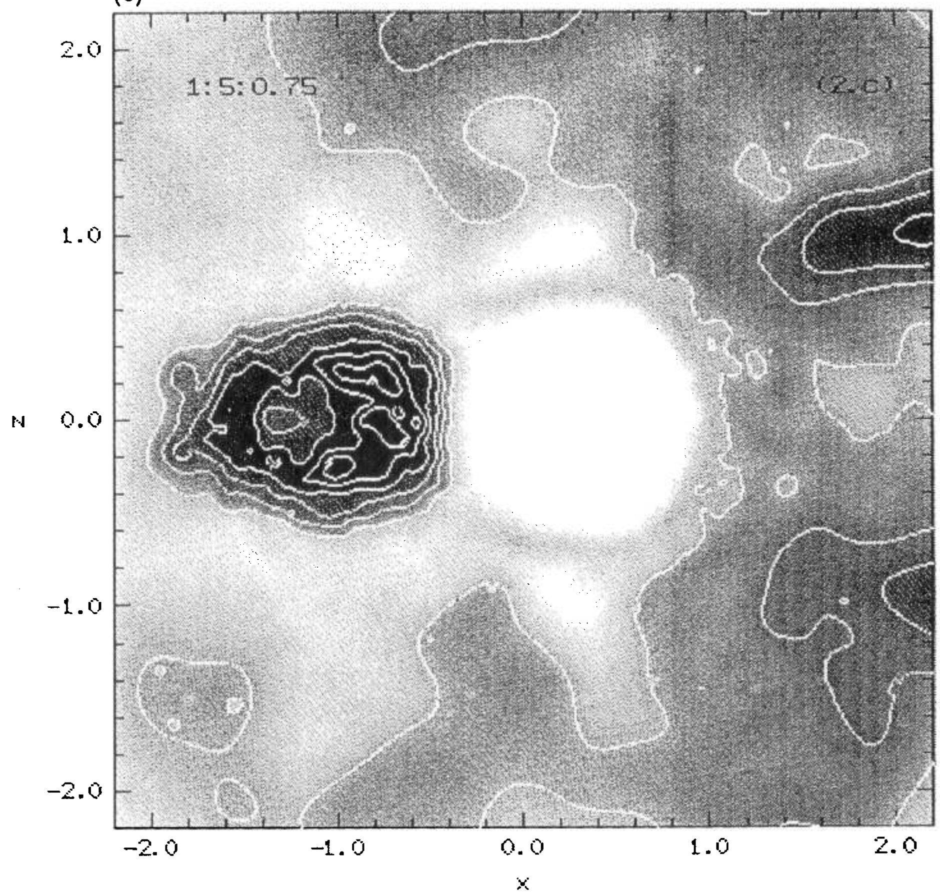

Figure 2 – *continued*

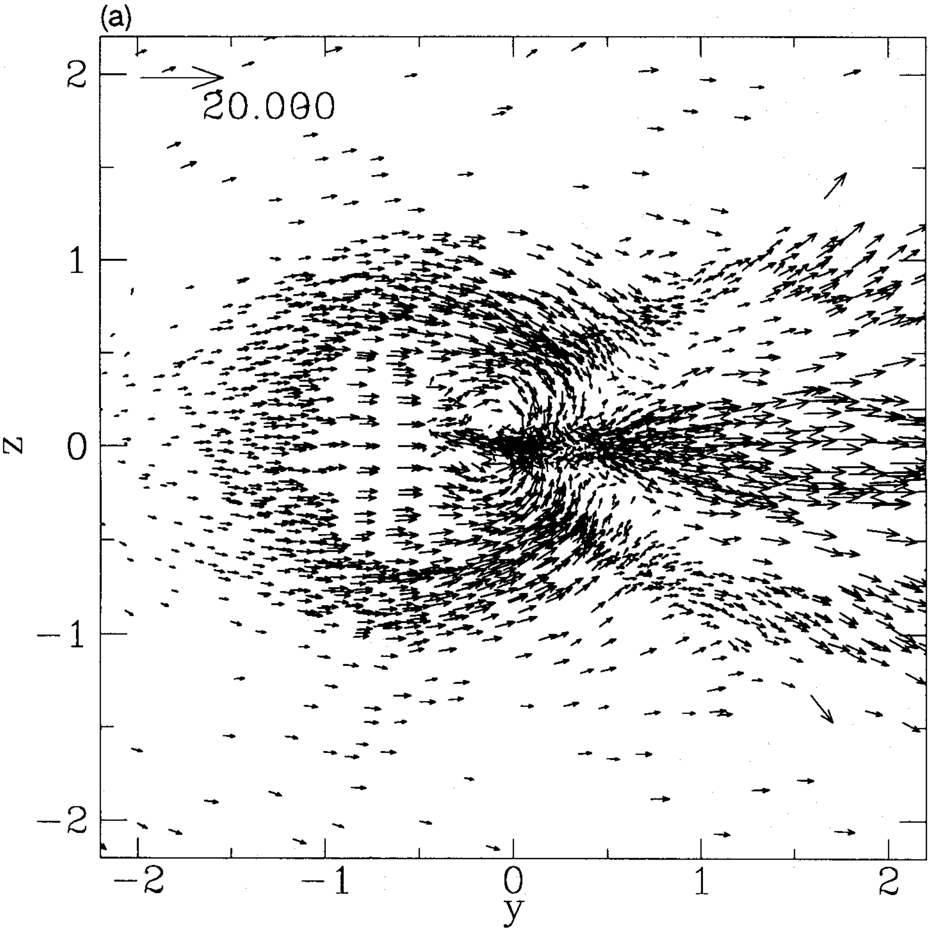

Figure 3. As Fig. 1 but for the (y–z) plane at the position of the accreting star ($x = -0.66$). (a) All particles in an x-slice of half-width 0.1 around the accreting star are shown. (b) Grey-scale from 0 to 1.5E-6.

Close to the secondary ($y = 0$), the temperature drops slightly as a result of the accretion boundary conditions specified there. Behind the object, $y > 0$, density and temperature drop only slowly.

Fig. 5(b) shows the line at $x = -0.66$, $y = 0.87$. Moving from negative to positive z, this line intersects the bow shock, the RL stream, and again the bow shock. In this bow shock, T and ρ increase sharply. Since the shock is oblique, however, the sonic line (where the Mach number $M = 1$) falls well within the shock. Fig. 6 shows Mach number contours superposed on a density grey-scale, illustrating this point (which was also observed in the simulations by Shima et al. 1985). Moving to larger y, the shock becomes more oblique and so sonic and shock lines separate further. Moving inwards to $z = 0$, density drops and temperature increases in the hot interior. This occurs at nearly constant pressure (Fig. 5b), which is expected since the z velocity component is subsonic due to the gas passing the bow shock. Between $z = -0.2$ and 0.2, we enter the RL stream. The temperature of the gas here is much lower, as explained before. The sequence bow shock – hot interior – RL stream is repeated in reverse order for $z > 0$.

In our SPH simulation, the resolution depends on the density, with higher density regions being better resolved. The interaction range h (equation 6) is a measure of the resolution, since all quantities are smoothed over a spherical region with radius $\approx 2h$. Fig. 7 shows this resolution in the orbital plane, allowing a comparison with the resolution attained by other authors. Close to the accreting star, the resolution is of the order of 0.06 behind the accreting star, and ≤ 0.09 in front of it, for the simulation with 40 000 particles. In the framework of the Bondi–Hoyle accretion, this resolution is often compared to the accretion radius $R_a = 2GM_2/v^2$, where in binary systems $v^2 = v_{orb}^2 + v_{wind}^2$ is the relative wind velocity. In our case, this radius is about 0.6 (the orbital separation being 1 in our units).

Studies of wind accretion from a 2D plane-parallel flow (see e.g. Livio 1992 for a review) often find that the stability of the flow depends on the size of the accreting object compared to R_a, the flow being usually stable for large objects ($\approx R_a/3$) and unstable for smaller objects ($\approx R_a/16$). Given the prescription for the accretion used in our simulation (see equation 7), the size of the accreting object is of the order of the resolution around it (i.e. about 1/11 at high resolution).

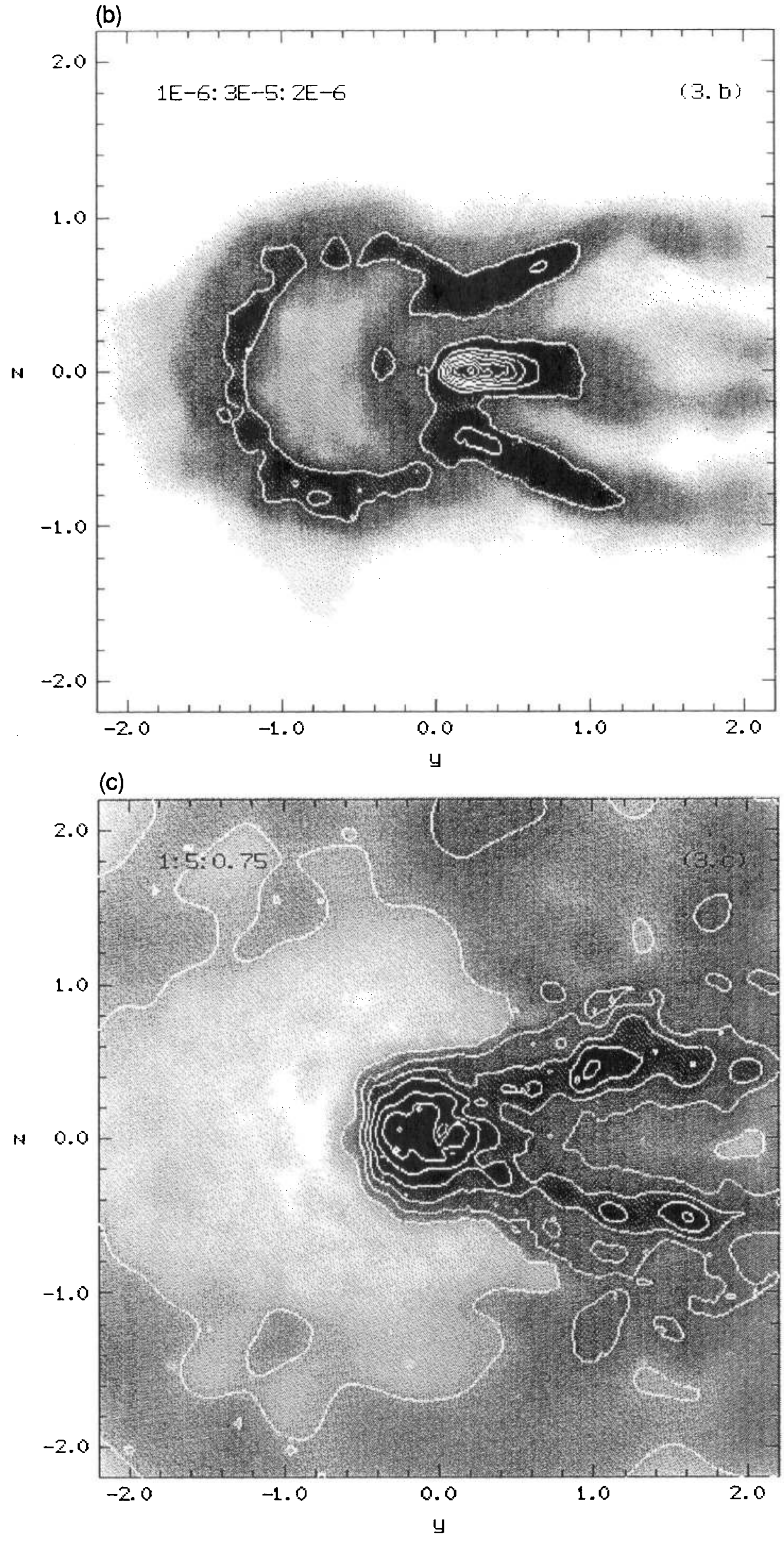

Figure 3 – *continued*

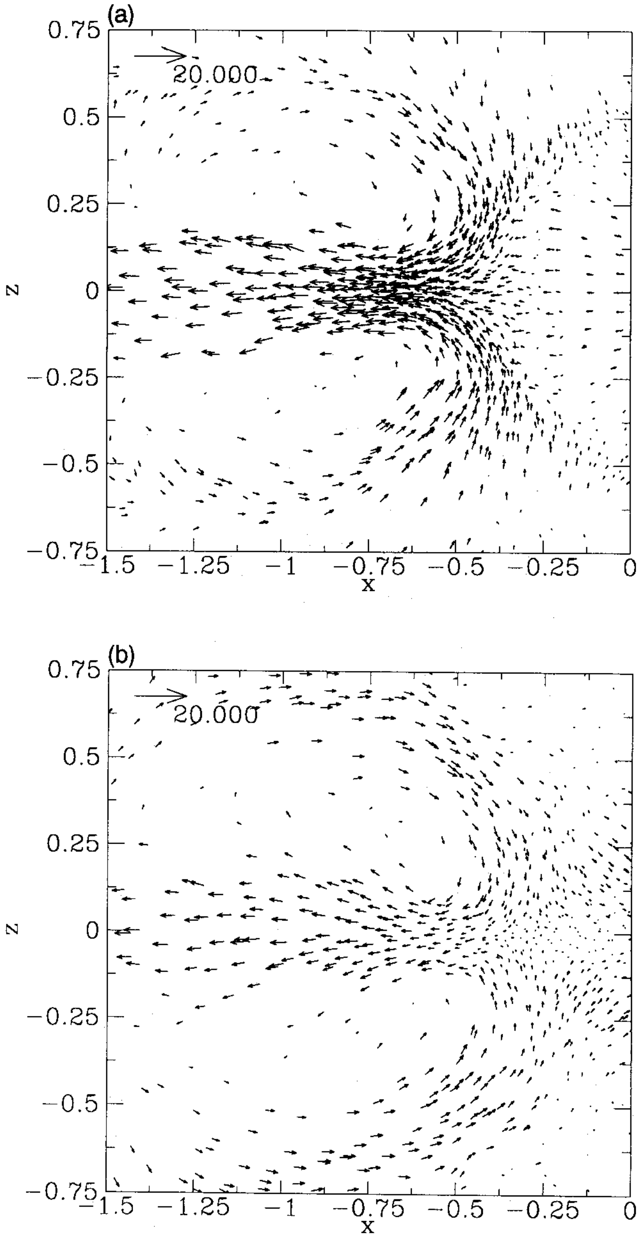

Figure 4. (a) The flow pattern in the $(x\text{–}z)$ plane for particles with $0.2 \le y \le 0.3$. (b) As (a) for particles with $0.5 \le y \le 0.6$.

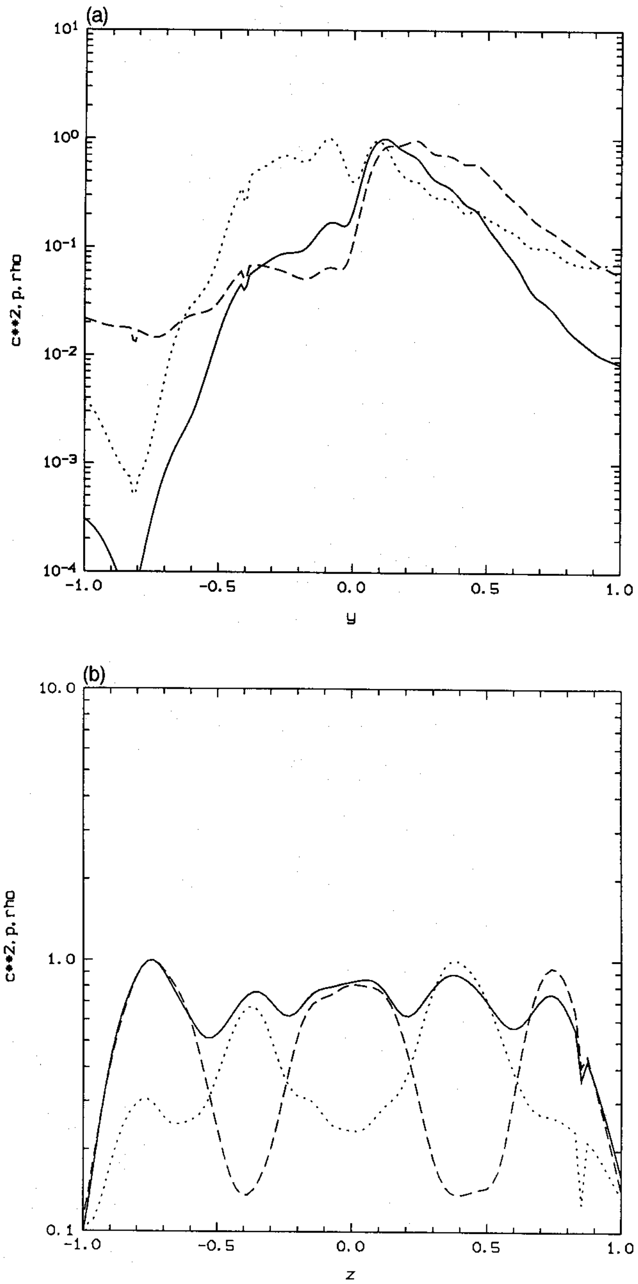

Figure 5. Cuts through the bow shock. (a) Cut along y $(x=-0.66, z=0)$ at the position of the accreting star. The pressure (solid line), sound speed squared (dotted line) and density (dashed line) are shown. These quantities are normalized by their maximum values along the considered line. (b) As (a) but along z at $(x=-0.66, y=0.87)$.

Although our resolution is only slightly coarser than that of the 2D calculations finding unstable flows, no instability is found over two orbital periods in our 3D simulation. This is well in line with other simulations (Boffin 1992; Matsuda et al. 1992), suggesting that instabilities are less violent in 3D flows. A key property in this respect may be the fact that the bow shock is detached in 3D, unlike in 2D (Livio 1992; Matsuda et al. 1992). One should note, however, that in the 2D calculations the instability sets in *at times large with respect to* R_a/c (≈ 4 in our case; c is the sound speed close to the accreting star), whereas our high-resolution simulation covered only two orbital periods (2 time units).

3.2 The isothermal model

Figs 8 to 10 show the structure of the isothermal flow in three different planes. The pattern differs quite substantially from that of the $\gamma=1.5$ case. As Fig. 8(b) shows, the flow is less smooth than in the previous model, with several knots of higher density forming. Fig. 8(a) shows that the bow shock and 'spiral arm' are still present (note that only 1/3 of all particles are shown to avoid crowding). The bow shock is no longer detached, as the pressure behind the shock is too low

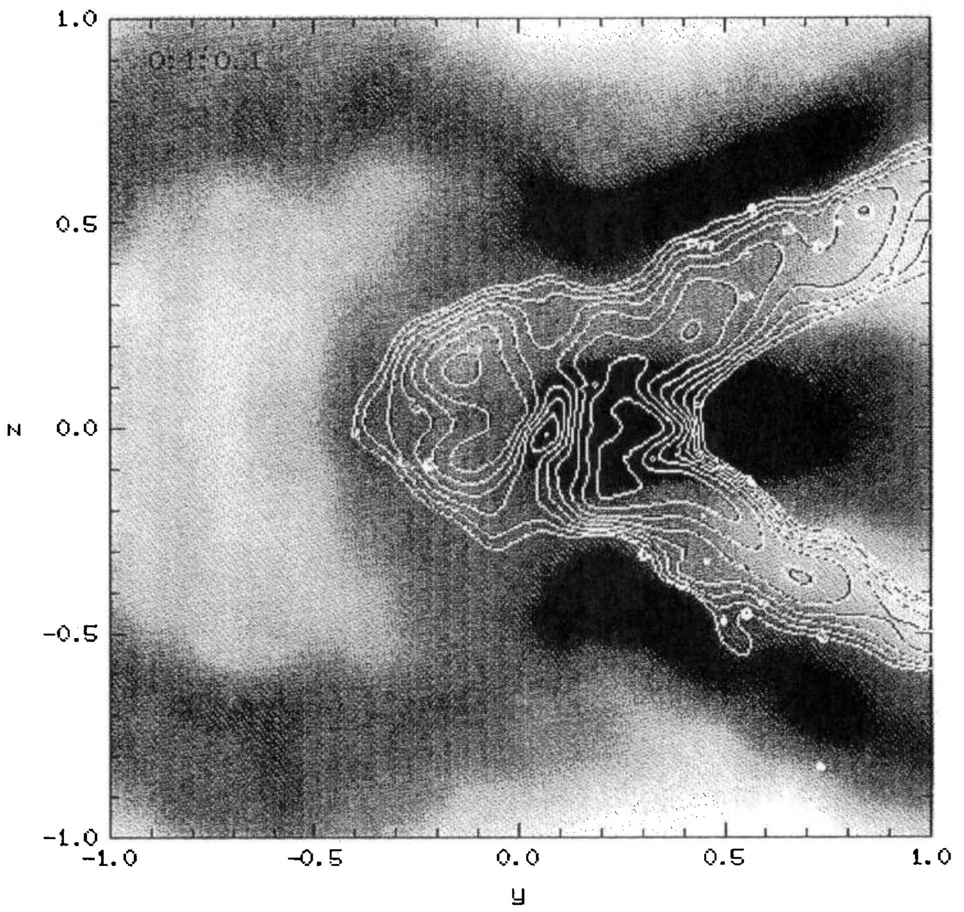

Figure 6. Grey-scale representation of the density in the $(y–z)$ plane showing the bow shock in the stationary frame. Contours of equal Mach number (considering only the velocity components in the plane) are superposed, ranging from 0 to 1 in steps of 0.1. The grey-scale is from 0 to 2E-6.

to support it against the ram pressure of the oncoming gas. The opening angle of the bow shock is much smaller (Fig. 10a). In front of the accreting star, gas is accelerated to higher velocities than in the previous model. As is evident from Fig. 8(a) an accretion disc forms around the secondary, with radius ≈ 0.3 and vertical extent ≈ 0.1.

As can be seen in the $x–z$ plane (Fig. 9), no vortex forms, unlike in the $\gamma = 1.5$ model. The dissipation introduced by the isothermal equation of state allows the gas to collapse into a disc instead. Gas can also be seen raining on to the disc from the low-density region above and below the plane.

Finally, Fig. 10 offers a view of the accretion cone in the $y–z$ plane. The thin accretion disc sticks out into the onrushing gas, which shocks into the accretion cone. Again note the small opening angle (compare with Fig. 3a). Fig. 11 shows a close-up view of the accretion disc and the flow pattern downstream from it.

The flow in the isothermal accretion wake is unstable, as can be seen from Figs 8(a) and 10(a) (seen in close-up in Fig. 11), in contrast to the adiabatic wake (Fig. 3a). The instability is probably caused by shear interactions between layers moving with different velocities in the wake (i.e. a Kelvin–Helmholtz instability; see Fig. 10a), and in addition by the interaction between the spiral-arm stream and the wake (Fig. 8a). This interaction is much stronger in the isothermal model than in the adiabatic one, because the adiabatic wake is shielded from the spiral-arm stream by a shock (Fig. 1a, the shock to the left of the accreting star at $x \approx -1.5$, $y \geq -0.2$), which is absent in the isothermal model.

Fig. 12 provides a closer look at the accretion disc in the $x–y$ plane. Fig. 12(a) shows that the disc is not circularly symmetric: it has an extension to the left, where gas in the disc collides with the nearly 'plane-parallel flow' in the y-direction, which causes the accretion cone. This figure moreover shows that the disc is fed from two sources: from a region to the right of the star $(x > -0.6)$, with gas coming directly from the mass-losing star (the RL stream), but also from the left $(x < -0.8)$. This gas comes from the spiral-arm stream, is slowed down in passing through the bow shock, and, in falling back on to the star, enters the disc. As Figs 12(b) and (c) show, the disc is not lying in the orbital plane. Note, however, that the initial state and the difference equations describing the time evolution of the flow have mirror symmetry with respect to the orbital plane. This implies that the origin of the tilt must be numerical round-off errors and may indicate that the *physical* disc is unstable to such a tilt.

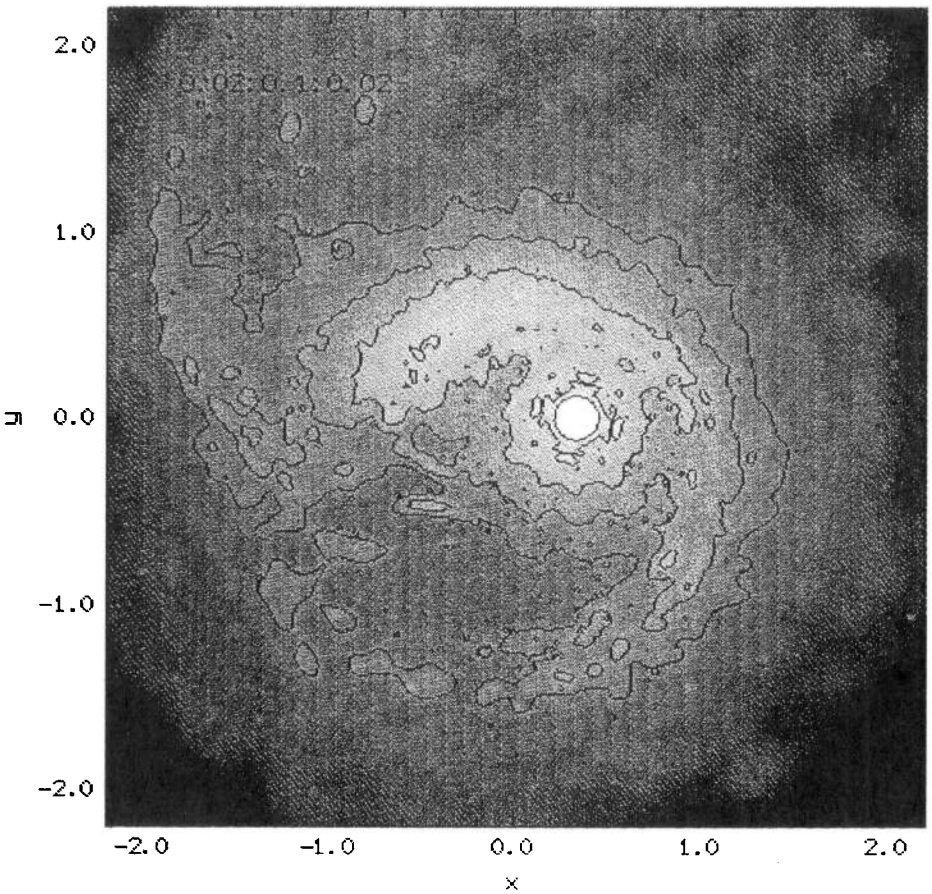

Figure 7. Grey-scale representation of the resolution length h (equation 6) for the simulation with 40 000 particles. The grey-scale ranges from 0 to 0.25. Contours ranging from 0.02 to 0.1 in steps of 0.02 are superposed.

The angular momentum of the disc is illustrated in Fig. 13. The total number of particles in the simulation increases from 20 000 to 40 000 over the time-span shown. Clearly, the disc is not well defined at the lower resolution. The mass of the disc seems to stabilize at $\approx 5\times10^{-6}$ (corresponding to $0.5\times10^{-6}\,M_\odot$), but this may well still depend on the resolution (the disc contains ≈ 4000 particles at the end of the run). Note that the angular momentum vector of the disc rotates in the stationary frame with the period of the binary. In the *inertial* frame, however, the rotation axis is nearly fixed (Fig. 13b). In this frame, the disc is wobbling: its behaviour is more complicated than simply precession and nutation.

Fig. 14 presents the velocity structure of the disc, which closely follows the predictions for orbits around a central object with a gravitational force smoothed according to the prescriptions of Section 2.2. This agreement indicates that the effect of the numerical viscosity is negligible in the disc. Non-zero radial velocities indicate that the orbits are slightly eccentric. Although in the innermost part of the disc all particles are spiralling inwards ($v_r<0$), being finally accreted, the signs of y and v_r are well correlated in the outer part of the disc. The sharpness of the inner boundary of the disc is a consequence of our prescription for mass accretion.

4 OBSERVATIONAL DIAGNOSTICS FOR WIND ACCRETION

4.1 High-temperature regions, cooling and hot radiation

Fig. 3(c) shows that high temperatures are reached in the vicinity of the accreting star in two different regions associated with the bow shock. The first one is upstream from the accreting object, where gas passes the bow shock at right angles. In this region, the highest temperatures are reached. The other region is the conical section between the accretion cone and the accretion column: since the gas passes the shock here obliquely, the temperatures reached are lower (by a factor of 3–4).

This high-temperature region in front of the accreting star has low density ($\rho\approx0.5\times10^{-6}$ or 10^{-15} g cm^{-3}) and is nearly spherical with radius ≈ 0.2. As shown in Fig. 5(a), the temperature increases by a factor of about 1000 in passing through the shock, reaching $\sim 60\,000$ K. This gas is a potential source of high-energy photons (UV and soft X-rays). We note, however, that the exact temperature of the gas will depend on the temperature in the red giant wind as well as on the efficiency of cooling processes, which were not included in the present simulations. The sound speed in the red giant

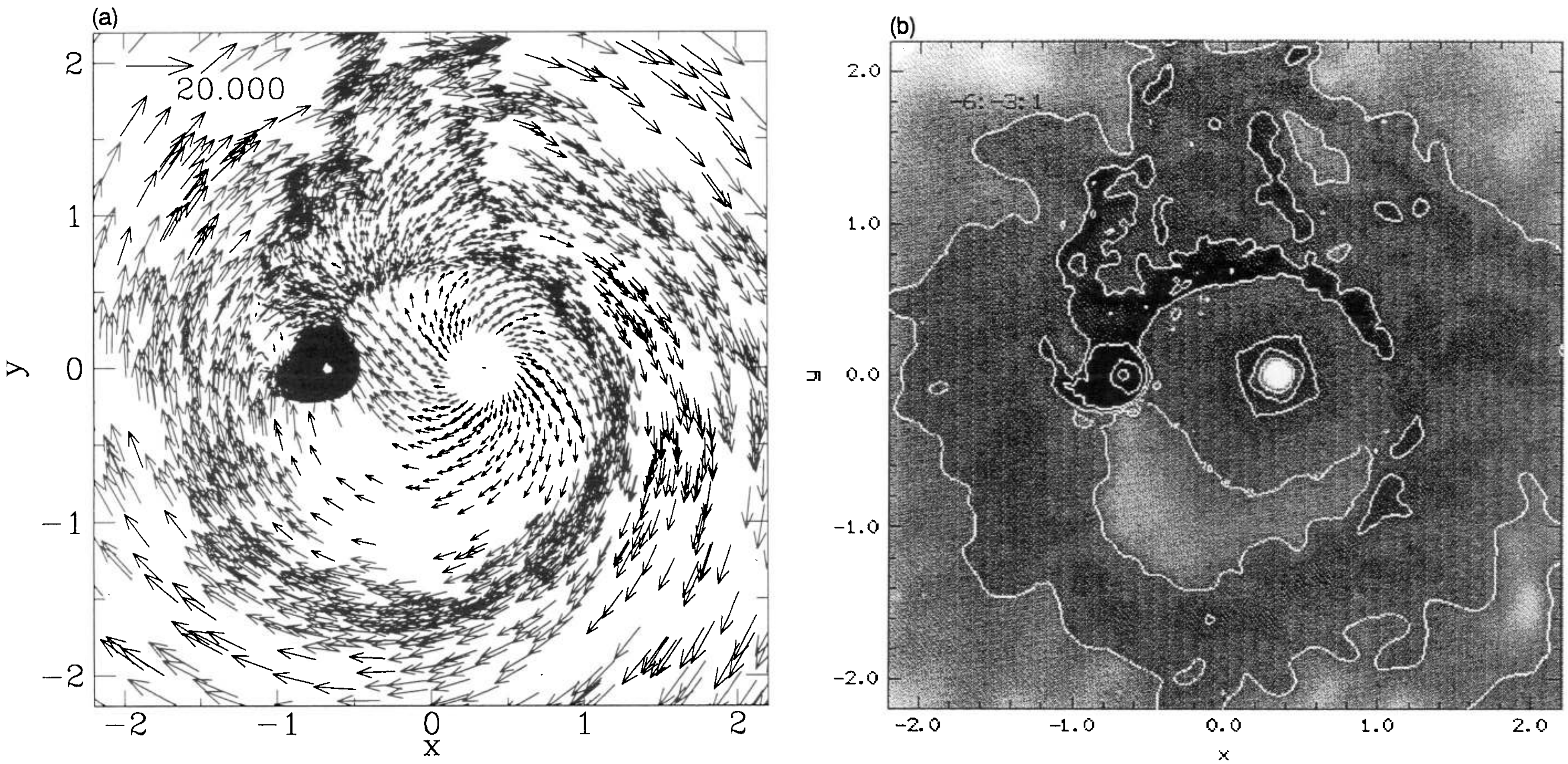

Figure 8. Flow structure in the stationary $(x-y)$ plane for the isothermal $\gamma=1$ model. The mass-losing star is at $(x=0.33,\ y=0,\ z=0)$, the accreting star at $(x=-0.66,\ y=0,\ z=0)$. (a) The velocity structure. The black structure around the accreting star is the accretion disc. 1/3 of all particles in the z-slice $[-0.1, 0.1]$ are shown. (b) Grey-scale representation of the logarithm of the density. The grey-scale ranges from -7.5 to -4. Logarithmic (base 10) contours are superposed.

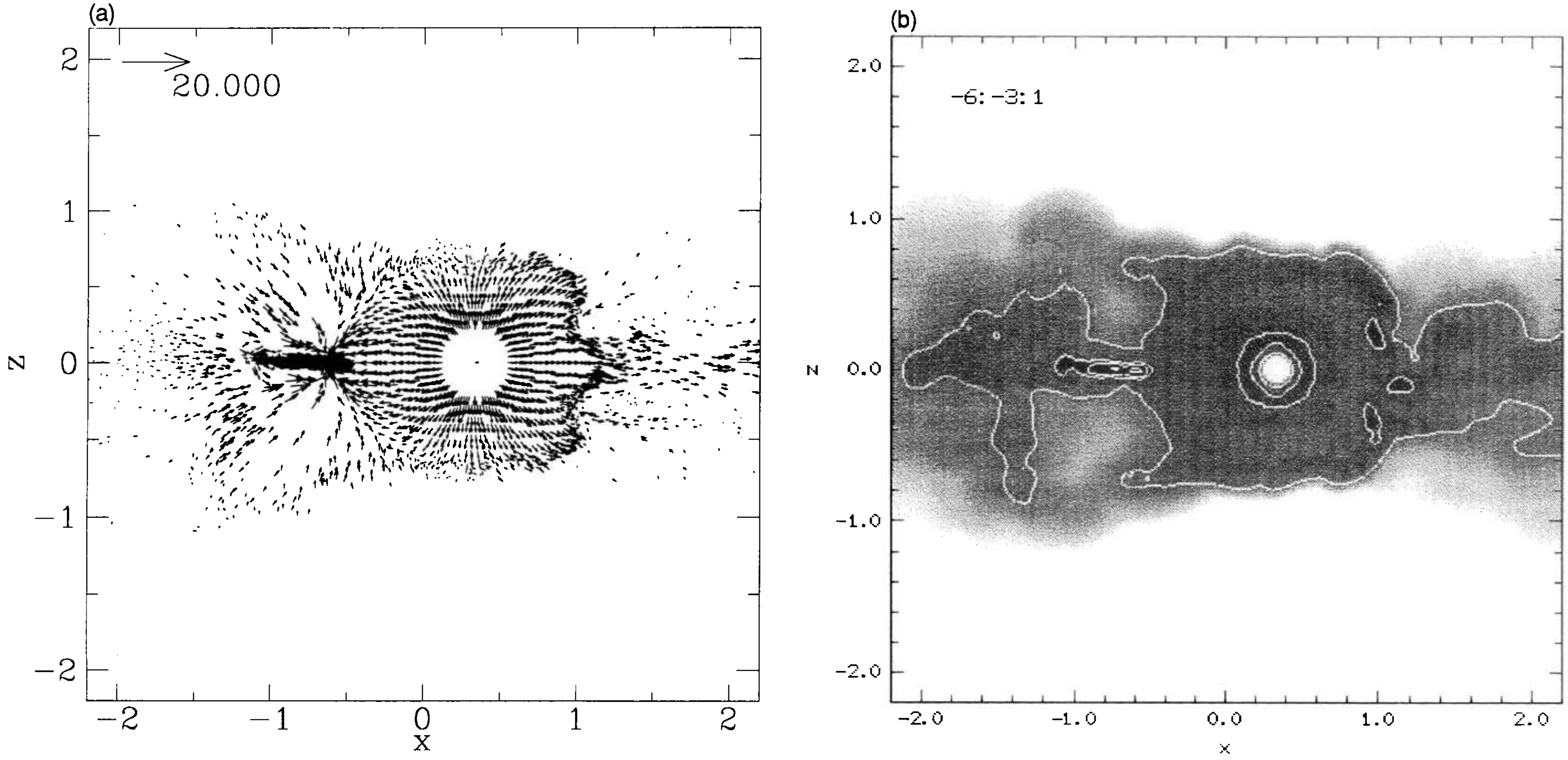

Figure 9. As Fig. 8 for the $(x\text{–}z)$ plane. (a) shows all particles in the y-slice $[-0.1, 0.1]$.

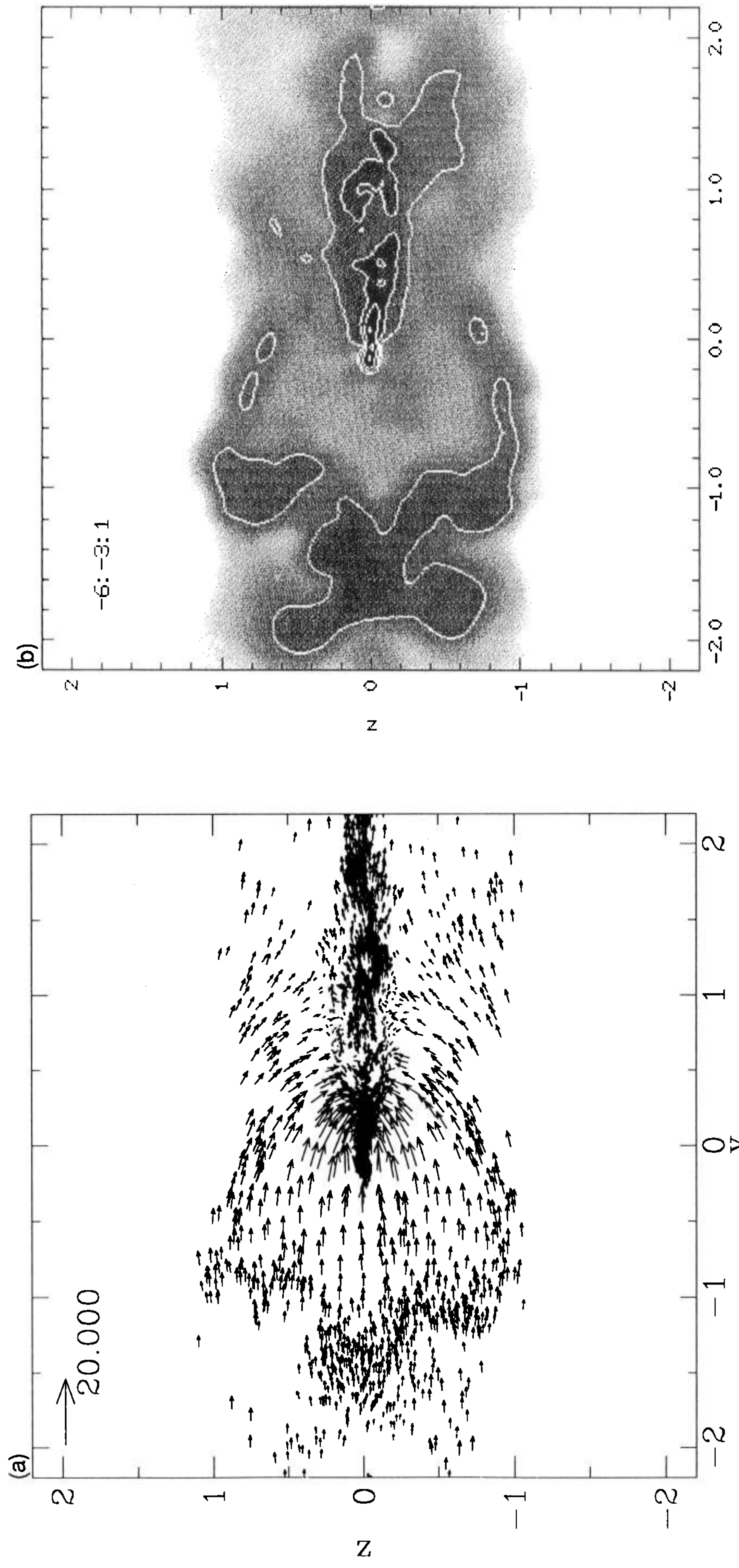

Figure 10. As Fig. 8 for the $(y$–$z)$ plane. (a) shows all particles in an x-slice of half-width 0.1 around the accreting star.

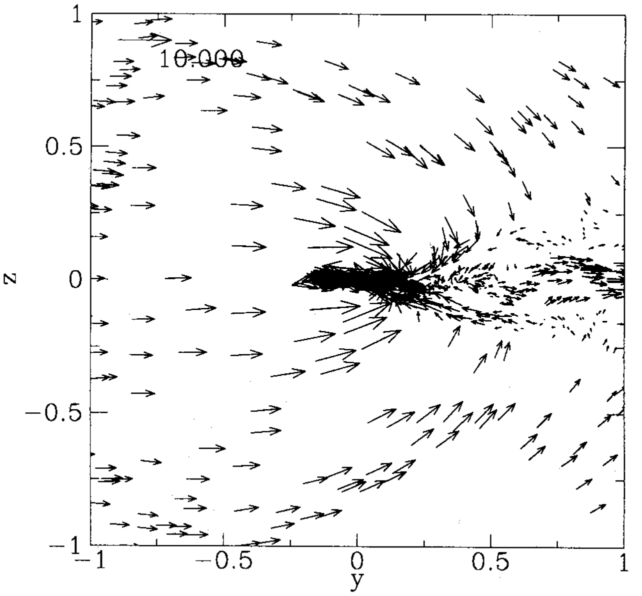

Figure 11. Close-up view of Fig. 10(a). The 'spiral-arm' stream enters from the left. The accreting star is at $y=z=0$. The accretion disc surrounds the star. The bow shock is to the right.

wind is 0.26 (corresponding to 114 K), so the wind is highly supersonic (Mach number = 10). However, the temperature behind the shock cannot be scaled in a simple way to more realistic values of wind temperature ($T_{\rm eff}\approx 3000$ K) because the strength of the shock (and hence the ratio of post- to pre-shock temperatures) depends on the initial temperature. Furthermore, cooling processes might also play an important role in the final temperature, as we now show. The importance of cooling can be assessed by comparing the cooling time-scale $\tau_{\rm cool}\approx u/L_{\rm cool}$ to the dynamical time-scale $\tau_{\rm d}=\Delta R/c$. Here, u is the thermal energy per unit mass, ΔR is the size of the high-temperature region, c is the sound speed and $L_{\rm cool}$ is the luminosity per unit mass. The cooling rate of a low-density, hot and optically thin plasma was computed for a solar composition by Raymond, Cox & Smith (1976). These authors take into account cooling from permitted, forbidden and semiforbidden line transitions, including contributions from dielectronic recombination, bremsstrahlung, radiative recombination and two-photon continua. The density is assumed to be low enough that collisional de-excitation is slower than the radiative decay of the excited ions. The rate by Raymond et al. (1976) assumes equilibrium cooling, whereas the gas flowing through the bow shock is likely to be out of equilibrium, which will increase the cooling rate. Typical values for the high-temperature region are $T\approx 10^5$ K, $\rho\approx 10^{-15}$ g cm^{-3}, $u\approx 1.4\times 10^{12}$ erg g^{-1}, $c\approx 10^4$ m s^{-1} and $\Delta R\approx 1.2$ au. These values and the emissivity read from fig. 1 of Raymond et al. (1976) yield $L_{\rm cool}\approx 1.6\times 10^{11}$ erg g^{-1} s^{-1}, corresponding to $\tau_{\rm cool}\approx 10$ s. Since $\tau_{\rm d}\approx 2\times 10^7$ s, cooling indeed plays an important role and should be included in future simulations. The high temperatures obtained in the adiabatic case therefore probably overestimate the actual values. The flow pattern itself might very well be affected by the inclusion of cooling, as is also hinted at by the large differences between the adiabatic and isothermal models. Since the isothermal case can be seen as a situation with infinitely fast cooling, the real situation is probably bracketed by our two models.

Since cooling is so efficient in the dense, hot bow shock region, one would expect the luminosity L of the cooling radiation to be a substantial fraction $f\lesssim 1$ of the total bulk kinetic energy flux $K\sim\rho v^3 A$ entering this region per unit time (ρ and v are the density and velocity of the gas entering the shock, and $A=\pi r^2$ is the surface area of the shock, which has radius r). Taking $\rho\approx 10^{-6}$, $v\approx 10$ and $r\approx 0.5$, we find $L\approx 0.2\,f\,{\rm L}_\odot$.

Although the present estimates of the temperatures and cooling luminosities associated with the adiabatic case must be considered rather crude, it is interesting to compare them with typical values found in interacting binary systems such as symbiotic or extrinsic S stars, where wind accretion is currently taking place. Several of the symbiotic systems are detached binaries containing K or M giants with a strong wind ($\dot{M}\gtrsim 10^{-6}$ M$_\odot$ yr^{-1}, Nussbaumer & Vogel 1987; Seaquist & Taylor 1990) and a main-sequence or WD companion. Orbital periods are of the order of several hundred days (Kenyon 1992). Extrinsic S stars have periods of the same order with WD companions (Johnson 1992; Jorissen & Mayor 1992), although they lose mass at a somewhat lower rate ($\dot{M}\lesssim 10^{-7}$ M$_\odot$ yr^{-1}, Jura 1988). The spectra of these interacting binaries are characterized by a wealth of UV emission lines of highly ionized atoms, mostly C, N, O, Si and Al (e.g. Nussbaumer & Stencel 1987; Johnson & Ameen 1991). These UV emission lines require a hot radiation source ($T\approx 10^5$ K) or some other kind of excitation mechanism (shock), whereas analyses of emission-line ratios indicate the presence of a nebula with electron densities 10^6–10^9 cm^{-3} and temperatures $(1-2)\times 10^4$ K (Nussbaumer & Vogel 1987, 1989; Nussbaumer & Stencel 1987). Typical C IV λ1550 line luminosities range from 10^{-2} L$_\odot$ in the interacting binary S star HD 35155 (Ake et al. 1991) to 1 L$_\odot$ in the prototypical wind-driven symbiotic system Z And (Fernández-Castro et al. 1988). We further note that the narrow Si III] and C III] lines observed by Ake et al. (1991) in the UV spectrum of HD 35155 have a radial velocity compatible with that of the accreting star if it is a WD (Jorissen et al. 1992). These lines could thus very well originate in the hot interior of the accretion cone downstream from the secondary, as described previously. Furthermore, since the hot gas is surrounded by a region of higher density (due to the obliqueness of the shock), high-density and high-temperature regions do not coincide. This configuration may give rise to the Fe II absorption lines observed in the UV spectrum of HD 35155. Overall, the UV continuum of HD 35155 radiates about 0.2 L$_\odot$, far too much for a WD but compatible with continuum radiation from the hot gas, as deduced from the values of the cooling luminosity obtained above.

The He I λ10830 line is very frequently observed in interacting binary systems, even in systems containing giants later than M0 (Brown et al. 1990), although in single giants it is only observed for spectral types earlier than K5–M0 (Zirin 1982; O'Brien & Lambert 1986). Since this line corresponds to the transition between the 2p ^{3}P^0 and 2s ^{3}S levels lying about 20 eV above the ground level, it needs energetic pumping (more precisely $kT\gtrsim 20$ eV or $T\gtrsim 2.3\times 10^5$ K). Since this line is observed in systems with a WD companion as well as in those with a main-sequence companion, the He I

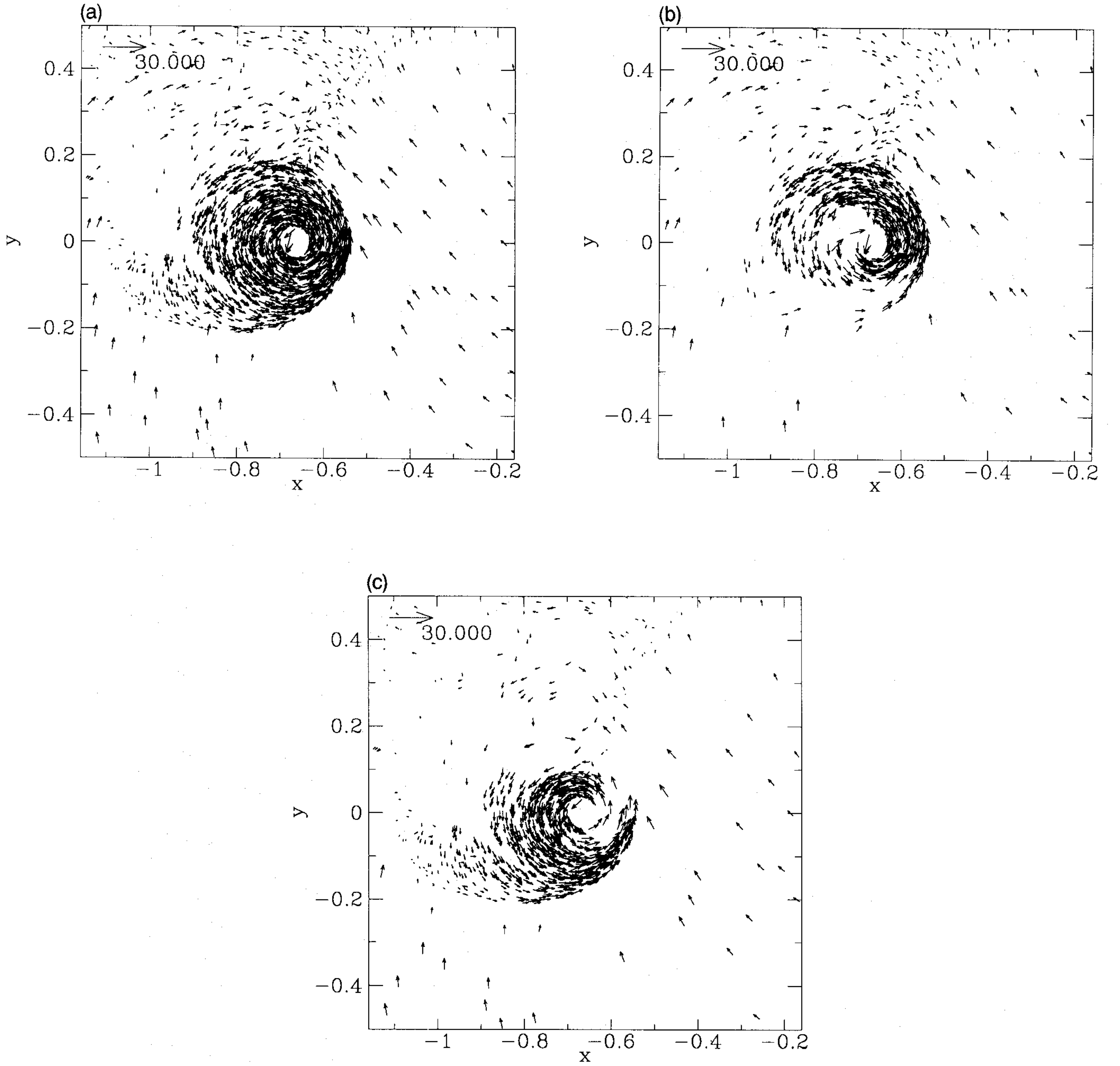

Figure 12. The accretion disc in the (x–y) plane. Note the two streams that feed the disc. (a) 1/3 of all particles in a z-slice $[-0.1, 0.1]$ of the orbital plane are shown. (b) As (a) but for the z-slice $[-0.1, 0]$. (c) As (a) but for the z-slice $[0, 0.1]$.

λ10830 line cannot be associated with the energy release of matter falling in the WD potential well. A very important clue to the origin of this line is provided by the observation by Shcherbakov & Tuominen (1992) that the variability of the He I λ10830 radial velocity and shape is compatible with the line being formed in the vicinity of the inner Lagrangian point. This provides a strong indication that this line may be associated with the hot bubble located upstream of the secondary.

X-rays, either hard or soft, were detected by *ROSAT* for several detached symbiotic systems (Bickert et al. 1992). X-ray luminosities in the 0.1–2.4 keV *ROSAT* band (not corrected for interstellar or circumstellar absorption) are in the range 10^{-3}–1 $L_{\odot}$.

In summary, although the temperatures found in our adiabatic simulation are too low to account for the X-ray emission in symbiotic systems, the cooling luminosity obtained is high enough to account for the observed UV line luminosities. We note that systems like CI Cyg that are believed to contain a main-sequence accretor are known to emit X-rays (Kenyon et al. 1991) so that this energy release cannot simply come from matter falling into the potential well of a WD.

4.2 The accretion disc

The possibility of forming an accretion disc during a wind accretion process has long been debated (Shapiro & Lightman 1976; Davies & Pringle 1980; Livio & Warner 1984; Livio et al. 1986; Sawada et al. 1989; Ho 1988), although always in the context of plane-parallel flow with or without a density gradient, thus closely following the traditional Bondi–Hoyle picture. The flow pattern obtained when binary rotation is taken into account is, however, quite different from the plane-parallel situation, especially when the wind velocity is of the same order as the orbital velocity, as it is in our case. We find the accretion disc to be fed from two sources, one being the gas stream coming directly from the primary star, the other the stream following the 'spiral arm', as described earlier. As can be seen in Fig. 8(a) (and in close-up in Fig. 12a), the binary rotation makes the feeding stream lag behind the accreting star, thus inducing the asymmetry required for the accretion of angular momentum. Although this situation is encountered in both the isothermal and adiabatic cases, an accretion disc only forms in the isothermal simulation, which differs only in the value of γ. In our opinion, this has the following explanation. In both cases gas is compressed by the gravitational force from the accreting star (we referred to this 'funnelling' earlier). When $\gamma = 1.5$, this heats up the gas so that the pressure increases so much that the gas stream expands vertically and is not confined in a disc. This expansion causes the vortex structure seen in Fig. 2(a). In the isothermal case, gas pressure does not increase so drastically and the gas stream does not expand so much: it stays in a disc. In a slightly different context, the simulations of Molteni, Belvedere & Lanzafame (1991) showed the increase in disc thickness with increasing γ, other parameters being the same. If this interpretation is correct, the formation of a disc will be determined by the efficiency of cooling (which determines the effective γ) and hence the value of the

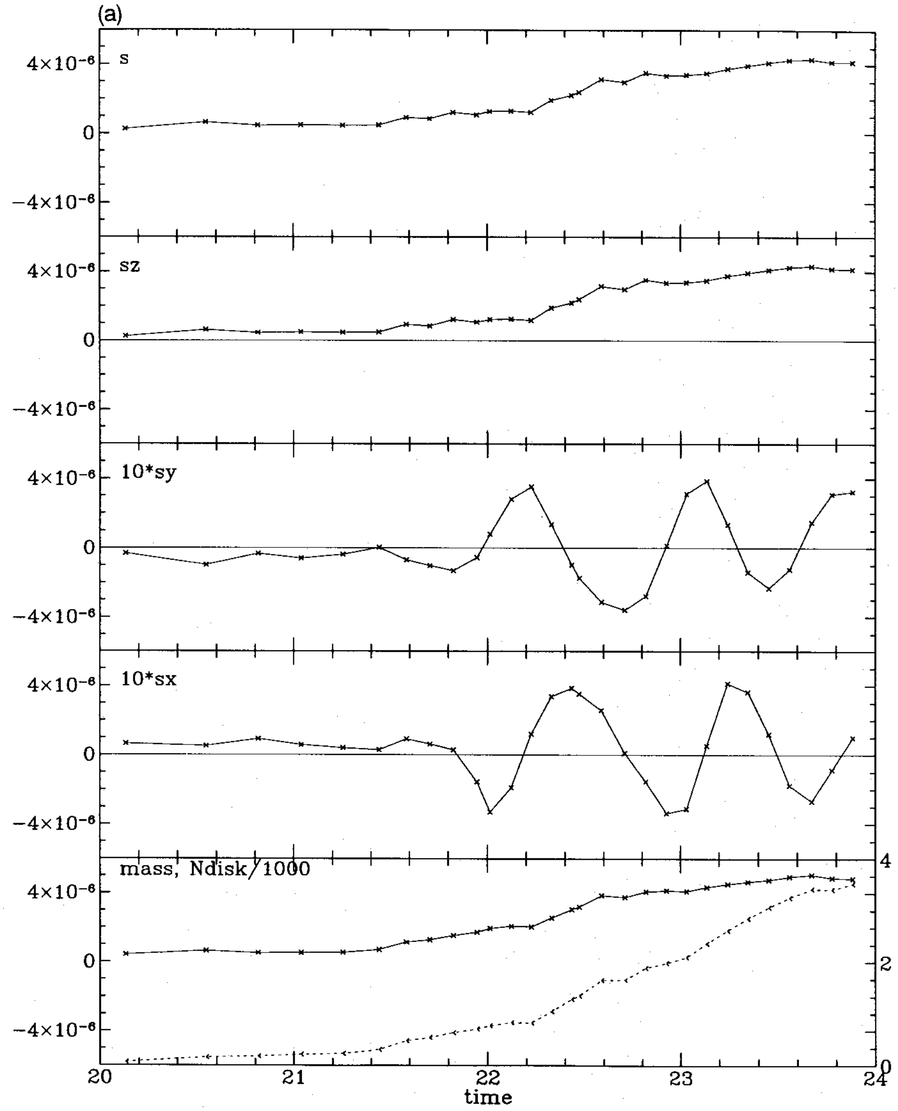

Figure 13. Spin momentum in the accretion disc in (a) the stationary frame, and (b) the inertial frame. From top to bottom are shown, as a function of time, the total spin; the spin along z; 10 times the spin along y; 10 times the spin along x; the total mass (solid line and left-hand scale), and the total number of particles in the disc (dotted line and right-hand scale).

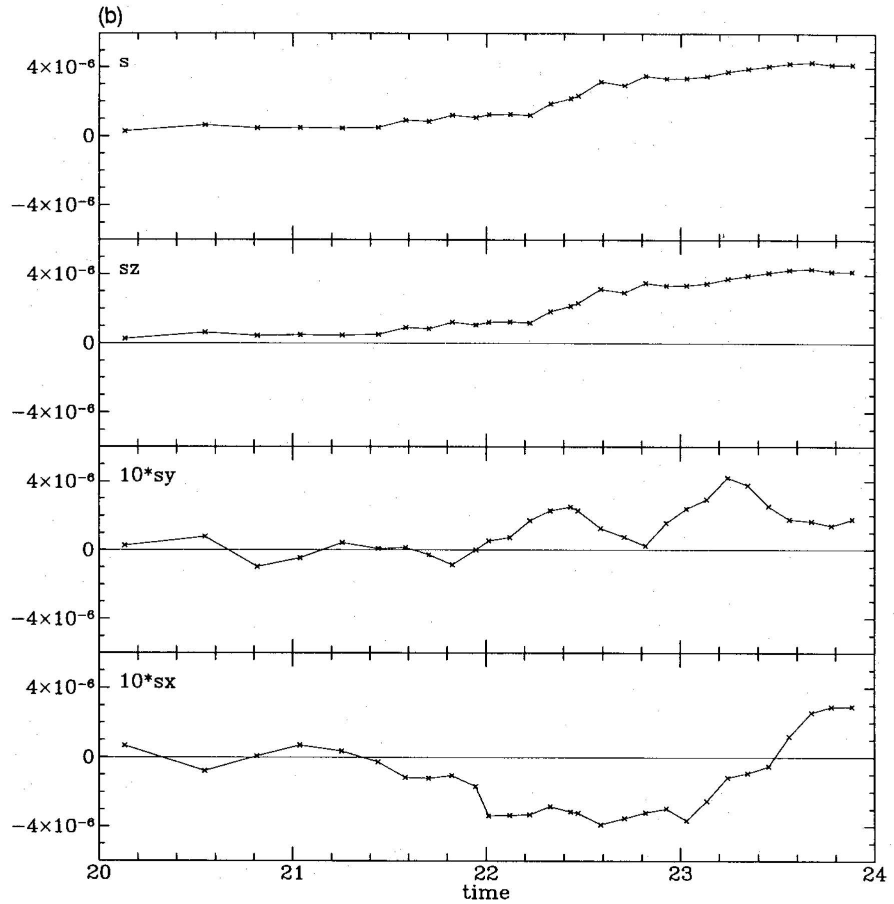

Figure 13 – *continued*

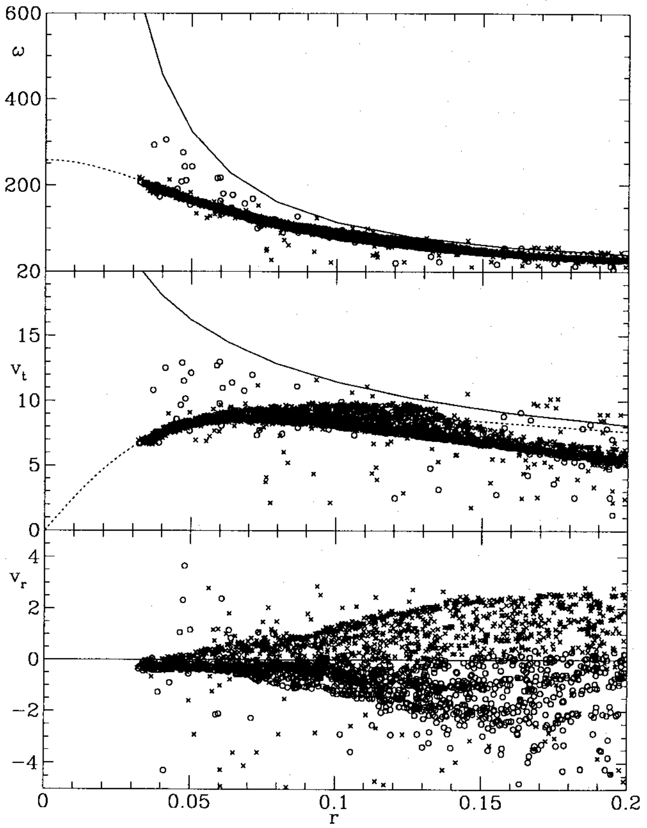

Figure 14. Rotation curve of the accretion disc. From top to bottom are shown the angular velocity, the tangential velocity and the radial velocity in the stationary frame. The solid line corresponds to a circular motion around a star with the same mass as the secondary. The dotted line includes the effect of smoothing the gravitational force (see Section 2.2). Open circles and crosses correspond to particles with $y<0$ or $y \geq 0$, respectively. Note the correlation between the signs of y and of v_r. The disc extends roughly to $r \sim 0.15$.

local density (recall that the cooling per unit volume is $\propto \rho^2$). In turn, the density will be determined by the mass-loss rate, the binary separation and the ratio of wind speed to orbital velocity. We would expect a disc to form for higher mass-loss rates, smaller binary separations and for wind speed and orbital velocity of the same order of magnitude.

As an example to which our simulation can be compared, Ake et al. (1991) observed a very broad C IV λ1550 line (FWHM ≥ 2500 km s^{-1}) in the interacting binary S star HD 35155, which they attributed to an accretion disc. In our simulation, the tangential velocities at the inner edge of the accretion disc amount to only some tens of km s^{-1} (Fig. 14). However, this value is limited by the resolution as well as influenced by the numerical smoothing we applied to the gravitational force of the secondary (see again Fig. 14). Assuming that particles follow Keplerian trajectories, the required velocities of the order of 1000 km s^{-1} would be reached at a radius of about 0.1 $R_\odot$ around a 0.6-$M_\odot$ accreting star, thus ruling out a main-sequence secondary. This further strengthens the case for WD companions around extrinsic S stars, already advocated by Johnson (1992) and Jorissen & Mayor (1992). Alternatively, this C IV line could be broadened by electron scattering in the hot bow shock region.

5 SUMMARY

We present 3D hydrodynamical simulations of wind-driven accretion flow in a binary system. The flow pattern is considerably more complicated than in the plane-parallel case. In the adiabatic $\gamma = 1.5$ model, a detached bow shock forms around the accreting star, and shows no sign of instability during the two orbital periods computed at high resolution. Post-shock temperatures are high enough to produce UV emission in this region. Such emission has in fact been observed in some such interacting binary systems. The gravitational force of the secondary causes a large compression of the gas that comes directly from the primary. This heated gas expands and gives rise to a vortex structure in a plane perpendicular to the orbital plane. In several parts of the flow, the cooling time is very short, hence more realistic simulations should include cooling.

The pattern in the isothermal case is quite different. Gas settles into a thin, nearly Keplerian accretion disc. This disc may be the source of the highly (rotationally) broadened lines observed in some interacting binary systems where wind accretion is believed to take place.

This paper is a first attempt to study wind accretion in a binary system through a fully 3D approach. Further studies should investigate the role in the flow structure of several parameters, such as that describing the wind acceleration or the accretion prescription, the ratio of wind to orbital velocities or the ratio of wind to sound velocities close to the mass-losing star. Situations where the mass-losing star rotates synchronously with the orbital motion, or where the orbit is eccentric, could also be considered.

ACKNOWLEDGMENTS

This work was begun while one of us (TT) benefited from an ESO studentship. We thank L. Lucy for a careful reading of an earlier version of the paper.

REFERENCES

Ake T. B., Johnson H. R., Ameen M. M., 1991, ApJ, 383, 842
Anzer U., Börner G., Monaghan J. J., 1987, A&A, 176, 235
Benz W., 1989, in Buchler J. R., ed., Numerical Modelling of Stellar Pulsations. Kluwer, Dordrecht, p. 269
Bickert K. F., Stencel R. E., Brugel E. W., Kenyon S. J., Fleming T. A., Schmitt J. H. M. M., 1992, A&A, submitted
Biermann P., 1971, A&A, 10, 205
Boffin H. M. J., 1992, in Kondo Y., Sisteró R. F., Polidan R. S., eds, Proc. IAU Symp. 151, Evolutionary Processes in Interacting Binary Stars. Kluwer, Dordrecht, p. 453
Boffin H. M. J., Jorissen A., 1988, A&A, 205, 155
Bondi H., 1952, MNRAS, 114, 195
Bondi H., Hoyle F., 1944, MNRAS, 104, 273
Bowen G. H., 1988, ApJ, 329, 299
Brown J. A., Smith V. V., Lambert D. L., Dutchover E., Jr, Hinkle K. H., Johnson H. R., 1990, AJ, 99, 1030
Davies R. E., Pringle J. E., 1980, MNRAS, 191, 599
de Kool M., Savonije G. J., 1988, A&A, 189, 331
Fernández-Castro T., Cassatella A., Giménez A., Viotti R., 1988, ApJ, 324, 1016
Gail H. P., Sedlmayr E., 1987, A&A, 171, 197
Gingold R. A., Monaghan J. J., 1977, MNRAS, 181, 375
Hernquist L., Katz N., 1989, ApJS, 70, 419
Ho C., 1988, MNRAS, 232, 91
Hockney R. W., Eastwood J. W., 1981, Computer Simulations using Particles. McGraw Hill, New York
Huang S. S., 1956, AJ, 61, 4
Hunt R., 1971, MNRAS, 154, 141
Johnson H. R., 1992, In Kondo Y., Sisteró R. F., Polidan R. S., eds, Proc. IAU Symp. 151, Evolutionary Processes in Interacting Binary Stars. Kluwer, Dordrecht, p. 157
Jorissen A., Mayor M., 1988, A&A, 198, 187
Jorissen A., Mayor M., 1992, A&A, 260, 115
Jorissen A., Sterken C., Manfroid M., Mayor M., 1992, Inf. Bull. Var. Stars No. 3730
Jura M., 1988, ApJS, 66, 33
Kenyon S. J., 1992, In Kondo Y., Sisteró R. F., Polidan R. S., eds, Proc. IAU Symp. 151, Evolutionary Processes in Interacting Binary Stars. Kluwer, Dordrecht, p. 137
Kenyon S. J., Oliversen N. A., Mikołajewska J., Mikołajewski M., Stencel R. C., Garcia M. R., Anderson C. M., 1991, AJ, 101, 637
Knapp G. R., Morris M., 1985, ApJ, 292, 640
Lattanzio J. C., Monaghan J. J., Pongracic H., Schwarz M. P., 1986, S.I.A.M. J. Sci. Stat. Comput., 7, 591
Livio M., 1992, in Kondo Y., Sisteró R. F., Polidan R. S., eds, Proc. IAU Symp. 151, Evolutionary Processes in Interacting Binary Stars. Kluwer, Dordrecht, p. 185
Livio M., Warner B., 1984, The Observatory, 104, 152
Livio M., Soker N., de Kool M., Savonije G. J., 1986, MNRAS, 222, 235
Lucy L. B., 1977, AJ, 82, 1013
McClure R. D., Woodsworth A. W., 1990, ApJ, 352, 709
Matsuda T., Inoue M., Sawada K., 1987, MNRAS, 226, 785
Matsuda T., Ishii T., Sekino N., Sawada K., Shima E., Livio M., Anzer U., 1992, MNRAS, 255, 183
Molteni D., Belvedere G., Lanzafame G., 1991, MNRAS, 249, 748
Monaghan J. J., 1985, Comput. Phys. Rep., 3, 71
Monaghan J. J., 1988, Comput. Phys. Comm., 48, 89
Monaghan J. J., Varnas R. S., 1988, MNRAS, 231, 575
Nussbaumer H., Stencel R. E., 1987, in Kondo Y., de Jager C., Linsky J. L., eds, Exploring the Universe with the IUE satellite. Kluwer, Dordrecht, p. 203
Nussbaumer H., Vogel M., 1987, A&A, 182, 51
Nussbaumer H., Vogel M., 1989, A&A, 213, 137
O'Brien G. T., Lambert D. L., 1986, ApJS, 62, 899
Paczyński B., 1971, ARA&A, 9, 183
Raymond J. C., Cox D. P., Smith B. W., 1976, ApJ, 204, 290
Savonije G. J., 1983, in Lewin W. H. G., van den Heuvel E. P. J., eds, Accretion-driven Stellar X-ray Sources. Cambridge Univ. Press, Cambridge, p. 343
Sawada K., Matsuda T., 1992, MNRAS, 255, 17P
Sawada K., Matsuda T., Hachisu I., 1986, MNRAS, 221, 679
Sawada K., Matsuda T., Anzer U., Börner G., Livio M., 1989, A&A, 221, 263
Seaquist E. R., Taylor A. R., 1990, ApJ, 349, 313
Shapiro S. L., Lightman A. P., 1976, ApJ, 204, 555
Shcherbakov A. G., Tuominen I., 1992, A&A, 255, 215
Shima E., Matsuda T., Takeda H., Sawada K., 1985, MNRAS, 217, 367
Sørensen S., Matsuda T., Sakurai T., 1975, Ap&SS, 33, 465
Tassoul J. L., 1987, ApJ, 322, 856

Theuns T., 1992, A&A, 259, 493
Theuns T., Rathsack M., 1993, Comput. Phys. Comm., 76, 141
Tout C. A., Hall D. S., 1991, MNRAS, 253, 9
Zirin H., 1982, ApJ, 260, 655

APPENDIX: NEIGHBOUR-SEARCHING ON A MULTI-GRID

To evaluate the sum in equation (6), one needs to find all particles j that satisfy

$$r_{ij}^2 \le (h_i + h_j)^2, \tag{A1}$$

where r_{ij} is the distance between particles i and j (we call j a neighbour of i if equation A1 is satisfied). In the standard linked-lists approach (for constant h), this is done as follows (e.g. Hockney & Eastwood 1981). A grid is placed over the whole of the computational domain, with cell size $2h$. One can now drastically reduce the number of particles j to observe by realizing that all potential neighbours of i are either in the same cell as i or in one of its (26, in 3D) neighbouring cells. The linked lists, which are set up in advance, allow one to identify efficiently all particles in a given cell.

This approach can still be used in the case where h is not constant, by using twice the *maximum* h as cell size. However, in a typical calculation, only a few particles (usually at the outer boundary) have such a large h and most of the others end up in only a few cells, which are filled with particles with small h. As a result, the scheme breaks down in what is effectively an N^2 search, which is what we started with. A large gain in efficiency can be obtained by using aligned multiple grids, with cell sizes differing by factors of one-half, starting with a grid with cell size $2h_{\max}$. All pairs of neighbours are now determined by looping over all grids, starting from the smallest one, at each step checking 13 (because of symmetry) cells of the same grid and all 26 neighbouring cells of all larger grids. The scheme requires storage of approximately $4n_g n_{\max}$ integers, where n_g is the maximum number of subgrids (we use $n_g = 7$), and $n_{\max}$ is the maximum number of SPH particles. In the present calculation, we obtained a speed-up of the calculation by more than a factor of 4.

We implemented this scheme to run on the Stardent GS 1000 computer at ESO. This computer has four MIMD vector processors which can work in parallel. We exploited this feature by parallelizing the calculation over cells (i.e. each processor is performing the calculation in a given cell) while the computation in one cell is vectorized. Parallelizing alone gives us a speed-up of nearly a factor of 3.8. We have since written another parallelized (over cells) SPH implementation based on a multi-grid for a SIMD parallel computer (Theuns & Rathsack 1993).